Decadal changes in atmospheric ammonia and dry deposition across China inferred from space-ground measurements and model simulations

Fan Sun[1], Yu Cui[1,2], Jiayin Su[3], Mark W. Shephard[4], Shailesh K. Kharol[4,5], Yifan Zhang[1,2], Xuejing Shi[1,2], Junqing Zhang[1,2], Huili Liu[1,2], Qitao Xiao[6], Xiao Lu[3], Zhao-Cheng Zeng[7], Timothy J. Griffis[8], Cheng Hu[1*]

[1] College of Ecology and Environment, Joint Center for sustainable Forestry in Southern China, Nanjing Forestry University, Nanjing 210037, China

[2] Yale-NUIST Center on Atmospheric Environment, Collaborative Innovation Center on Forecast and Evaluation of Meteorological Disasters (CIC-FEMD), Nanjing University of Information Science & Technology, Nanjing, 210044, China

[3] School of Atmospheric Sciences, Sun Yat-sen University, Zhuhai, 519082, China.

[4] Environment and Climate Change Canada (ECCC), Toronto, Ontario, M3H 5T4, Canada

[5] AtmoAnalytics Inc., Brampton, Ontario, L6S 6L2, Canada

[6] Key Laboratory of Lake and Watershed Science for Water Security, Nanjing Institute of Geography and Limnology, Chinese Academy of Sciences

[7] School of Earth and Space Sciences, Peking University, Beijing 100871, China

[8] Department of Soil, Water, and Climate, University of Minnesota-Twin Cities, Minneapolis, MN, USA

*Corresponding author: Cheng Hu (chenghu@njfu.edu.cn or nihaohucheng@163.com)

Abstract: Ammonia (NH_3), a key alkaline gas in the atmosphere, significantly influences ecosystem nitrogen cycling and the formation of fine particulate matter ($PM_{2.5}$). However, limited ground-based monitoring hinders understanding of NH_3's spatial and temporal dynamics and its dry deposition across China, which is ranked as one of the largest global NH_3 emission hotspots. This study integrated 2013-2023 satellite-derived NH_3 column concentrations from the Cross-track Infrared Sounder (CrIS) with adjustments from approximately five years ground in-situ ground observations to derive spatial-temporal variation in ground-level NH_3 concentrations across China. We also used the GEOS-Chem transport model and a random forest algorithm by using emission inventories and reanalysis meteorological fields to simulate NH_3 dry deposition velocity and fluxes, and explore the mechanisms driving observed trends. The CrIS observations results show that column-averaged (averages from ground to ~1 km) NH_3 concentrations were the highest in the North China Plain (>10 ppb), with notable annual and seasonal increasing trends. NH_3 concentrations in 2023 were 13.8%-30.6% higher than in 2013. CrIS retrievals aligned well with in-situ data, though were generally about twice as high. After applying the regression equation between ground in-situ observations and CrIS column-averaged NH_3 concentrations, we derive the spatial-temporal ground-level (1~1.5 m) NH_3 concentrations and dry deposition fluxes from 2013 to 2023. The NH_3 dry deposition fluxes exhibited a clear east-west gradient, with maxima in the North China Plain, and another hotpot region is also observed in the Sichuan Basin, southwestern China. Increases in ground-level NH_3 concentrations and deposition were most pronounced in urban, cropland, and forest regions, with urban areas experiencing the fastest growth and grasslands the highest total deposition. The national mean ground-level NH_3 concentration and dry deposition flux were 4.98 ppb and 0.51 g NH_3 m^{-2} yr^{-1}, respectively. Anthropogenic emissions explained 77.4% of the variability in ground-level NH_3 concentration trend, and meteorological factors accounted for the remainder. Besides, 72.6%-81.2% of the NH_3 dry deposition trend was governed by NH_3 concentration changes. This study identifies the underlying cause of increasing ammonia pollution, which can be used to better inform nitrogen management strategies in China.

Keywords: NH_3 concentration, dry deposition, satellite-based observation, random forest model

1 Introduction

Ammonia (NH_3), as the most abundant alkaline gas in the atmosphere, readily reacts with acidic species such as nitric acid and sulfuric acid to form secondary inorganic aerosols. These aerosols contribute significantly to fine particulate matter ($PM_{2.5}$), thereby adversely affecting human health, air quality, and atmospheric visibility (Na et al., 2007; Hauglustaine et al., 2014; He et al., 2001). Reducing NH_3 emissions has been identified as a cost-effective strategy for mitigating air pollution (Pinder et al., 2007; Wu et al., 2016). In addition, excessive atmospheric NH_3 can also deposit onto terrestrial and aquatic ecosystems through dry and wet processes, leading to soil acidification, eutrophication, and biodiversity loss (Hernández et al., 2016; Fu et al., 2017; Hu et al., 2021). Therefore, monitoring and quantifying atmospheric NH_3 concentrations and deposition rates within different land cover types, especially at global emission hotspots, are critical for informing nitrogen management strategies and protecting air, soil, and water resources, as well as human health (Liu et al., 2017a; Griffis et al., 2019).

As the world's largest agricultural country in terms of total crop yield, China is also among the top NH_3 emitters globally. In 2018, the global NH_3 emissions from rice, wheat and corn fields were 4.3 ± 1.0 Tg N yr^{-1}, of which China's emissions per unit area were as high as 19.7 kg N ha^{-1} yr^{-1}, which was much higher than that of the United States (9.1 kg N ha^{-1} yr^{-1}) and India (10.8 kg N ha^{-1} yr^{-1}) (Zhan et al., 2020; Luo et al., 2022). From global inventories such as EDGAR and CEDS, China's NH_3 emissions accounted for 19.8% of the global total in 2013. In 2022, this proportion had declined to about 14.5% (Crippa et al., 2024). In recent years, the proportion of NH_3 deposition to total nitrogen (N) deposition has increased steadily, accounting for approximately 67.0% in China in 2020 (Liu L et al., 2024). This upward trend is expected to continue, driven by declining NO_x and SO_2 emissions due to pollution control policies and rising NH_3 emissions associated with global agricultural intensification (Erisman et al., 2008; Goldberg et al., 2021; Pinder et al., 2008).

NH_3 deposition in China is nearly double that of the EU (Liu L et al., 2024), mainly due to excessive nitrogen fertilizer application. In 2014, agricultural NH_3 volatilization accounted for

88 12 Tg N yr^{-1} globally, with China contributing about 34% (Ma et al., 2020). Anthropogenic

89 activities have nearly doubled NH$_3$ emission over the past few decades, with cropland and

90 livestock sources making up around 80% of the global total emissions. Non-agricultural

91 sources—such as wildfire biomass burning, wastewater treatment, human excreta, and

92 transportation—remain relatively minor (Behera et al., 2013; Zhu et al., 2015; Van Damme et

93 al., 2018; Lutsch et al., 2019). Although the growth rate of both agricultural and non-agricultural

94 NH$_3$ emissions in China has slowed in recent years, the absolute emissions continue to rise

95 (Chen J et al., 2023).

96

97 Atmospheric NH$_3$ concentration serves as a key indicator of emission intensity due to its

98 relatively short atmospheric lifetimes, typically the order of hours in the atmospheric boundary

99 layer (hereafter ABL) (Evangeliou et al., 2021). Therefore, accurately quantifying its

100 spatiotemporal variations and identifying the underlying drivers is essential for constraining

101 NH$_3$ emission estimates, evaluating the ecological and environmental impacts and informing

102 effective mitigation strategies. Due to its high reactivity and predominant agricultural sources,

103 NH$_3$ exhibits pronounced temporal and spatial variability. To date, China operates two national

104 observation networks dedicated to monitoring NH$_3$ concentrations and deposition: The National

105 Nitrogen Deposition Monitoring Network (NNDMN, established in 2004) and the Ammonia

106 Monitoring Network of China (AMoN-China, established in 2015). While these networks

107 provide high-quality measurements, their sparse spatial coverage limits their ability to

108 characterize regional patterns for China (Liu et al., 2017a; b). Additionally, few sites offer long-

109 term (>10 years) continuous data records (Wang et al., 2023), posing challenges for trend

110 analysis across China. The limited availability of NH$_3$ monitoring data impedes our

111 understanding of its spatial-temporal patterns and impacts on air quality, climate, and

112 ecosystems.

113

114 In addition to surface monitoring, the chemical transport models (CTMs, i.e. GEOS-Chem,

115 WRF-Chem) are widely used to simulate NH$_3$ concentrations and dry deposition, as they

116 incorporate processes such as emission, transport, deposition, and chemical transformation (Hu

117   et al., 2020; 2021; Lu et al., 2020). However, their accuracy is constrained by uncertainties in

118   emission inventories and model parameterizations (e.g. bi-directional flux), where the bias in

119   both NH_3 emissions and other species (e.g. NO_x and SO_2) can lead to considerable uncertainty

120   in simulating NH_3 concentration and corresponding deposition to ground (Kharol et al., 2018;

121   Van Der Graaf et al., 2022; Liu S et al., 2024). NH_3 emission estimates remain highly uncertain

122   due to outdated activity data, poorly constrained emission factors, and underrepresented sources

123   such as cities (Chang et al., 2021). Compared to most other air pollutants, NH_3 exhibits greater

124   variability and uncertainty in different inventories and models, particularly because of its

125   diverse agricultural sources and large influence from meteorological factors and human

126   activities (Beusen et al., 2008; Behera et al., 2013).

127

128   Recent advances in satellite remote sensing offer new opportunities to monitor boundary layer

129   atmospheric NH_3, which was first demonstrated by Beer et. al., (2008) with NASA's

130   Tropospheric Emission Spectrometer (TES) observations. The first global NH_3 distribution map

131   was derived in 2009 using data from the Infrared Atmospheric Sounding Interferometer (IASI)

132   onboard the MetOp-A satellite (Clarisse et al., 2009). Since then, other hyperspectral infrared

133   instruments have been used to map NH_3 concentrations over large regions, such as NASA TES

134   sensor, NASA/NOAA Cross-track Infrared Sounder (CrIS), the NASA Atmospheric Infrared

135   Sounder (AIRS), JAXA Greenhouse Gases Observing Satellite (GOSAT), and the

136   Geostationary Interferometric Infrared Sounder (GIIRS) on board China's FengYun-4B satellite

137   (Shephard et al., 2011; Shephard et al., 2015; Someya et al., 2020; Chen J et al. 2023; Zeng et

138   al., 2023). Satellite observations provide wide spatial coverage and continuous temporal

139   resolution, helping to fill spatial-temporal observation gaps by ground networks. Satellite-

140   derived NH_3 retrievals contain approximately 1 independent piece of information driven by

141   peak sensitivity (averaging kernel) in the ABL (~1-3 km) (Shephard et al., 2011; Shephard et

142   al., 2020) that can be represented as profiles with limited vertical resolution or integrated

143   column-averaged values. Therefore, column-averaged satellite retrievals cannot directly

144   replace ground-level (1~1.5 m) concentrations but provide complementary information that

145   helps fill in monitoring gaps.

146 Despite these limitations, satellite observations have been increasingly used to constrain NH_3

147 emissions, assess deposition flux, and identify trends (Chen et al., 2021; Kharol et al., 2018;

148 Van Damme et al., 2021). For instance, Liu L et al. (2019) estimated global surface NH_3

149 concentrations from IASI data and identified high concentrations (>6 μg N m^{-3}) in the North

150 China Plain and northern India. Linear trend analysis from 2008 to 2016 revealed strong

151 increases in eastern China (>0.2 μg N m^{-3} yr^{-1}). More recently, satellite data have been used to

152 investigate urban NH_3 concentrations globally, showing a significant rise (1.2% yr^{-1}) in 2008-

153 2019 (Liu S et al., 2024). These studies demonstrate the utility of satellite retrievals in

154 characterizing NH_3 pollution and its spatiotemporal evolution, especially in regions lacking

155 surface monitoring. In addition to these near surface ammonia concentration observations (from

156 either in-situ surface or satellite observations), the dry deposition estimations also depend on

157 deposition velocities (Lei et al., 2021; Liu S et al., 2024). Therefore, an alternative and reliable

158 approach is to combine model simulated dry deposition, ground-level NH_3 concentration from

159 sites and satellite-based column-averaged observations, which can make full use of

160 corresponding advantages and eliminate the large uncertainty from emission inventories of

161 different pollution species.

162

163 Therefore, accurate estimation of NH_3 dry deposition and its driving factors are becoming

164 increasingly critical. Kharol et al. (2018) reported that NH_3 contributed more than NO_2 to dry

165 N fluxes over much of North America in the warm season. Liu L et al. (2019) used satellite-

166 derived data to estimate global NH_3 dry deposition during 2008-2016, with results broadly

167 consistent with ground measurements, highlighting the potential for satellite-based NH_3

168 observations to fill spatial-temporal gaps in NH_3 deposition assessment. In China, satellite

169 observations indicate that elevated NH_3 concentrations are predominantly observed in the North

170 China Plain, Northeast China, and the Sichuan Basin, whereas lower concentrations are found

171 on the Tibetan Plateau (Liu et al., 2017b). Despite the prominent NH_3 pollution identified in

172 several regions of China, there remains a lack of comprehensive long-term studies that examine

173 the spatiotemporal variations of NH_3 concentrations and dry deposition. The key drivers behind

174 these variations—impacted by rapid urbanization, land-use changes, climate change, and shifts

in fertilizer application practices—have not been sufficiently quantified. While observational studies conducted over a ten-year period cannot fully address the data gap, they offer valuable insights into the medium- and long-term trends in NH_3 concentrations and deposition patterns. To robustly constrain and quantify the spatiotemporal variations in column-averaged near surface level (average from ground to ~1 km), ground-level (1~1.5 m) NH_3 concentrations and dry deposition over the past decade, we integrated multiple data sources and analytical approaches. These included high-resolution satellite-derived NH_3 retrievals from 2013 to 2023, ground-based observational datasets, simulations from the GEOS-Chem chemical transport model, and dry deposition velocity estimates derived using a random forest algorithm. This study aims to address the following key scientific questions: (1) What are the spatial and temporal patterns of near surface level and ground-level NH_3 concentrations across different land cover types in China over the past decade from 2013 to 2023? (2) What are the temporal trends in NH_3 dry deposition across China during this period, and what are the primary driving factors? (3) What are the NH_3 concentrations and dry deposition fluxes in China compared to those in other regions globally? By addressing these questions, this study seeks to advance understanding of the nitrogen cycle in China and provide a scientific foundation for evaluating ecological impacts and informing targeted strategies for nitrogen management and sustainable agriculture.

2 Materials and Methods

2.1 Satellite-based atmospheric NH_3 concentration

The CrIS (version 1.6.4) satellite-based atmospheric NH_3 concentration used in this study. The CrIS is a hyperspectral infrared sounder onboard the Suomi National Polar-orbiting Partnership (Suomi NPP), NOAA-20, and NOAA-21 satellites (Shephard et al., 2020). Operating in a sun-synchronous orbit at an altitude of approximately 824 km, CrIS provides global coverage twice daily, with local overpass time around 13:30 (daytime) and 01:30 (nighttime). The instrument has a swath width of up to 2200 km, with a nadir spatial resolution of approximately 14 km, and excellent signal-to-noise ratio (Zavyalov et al., 2013). The CrIS fast physical retrieval (CFPR) algorithm (Shephard and Cady-Pereira, 2015) produces NH_3 retrievals using CrIS

204 onboard Suomi NPP from May 2012 to May 2021, and CrIS onboard NOAA-20 since March

205 8, 2019.

206

207 In this study, the near surface level of CrIS-derived atmospheric NH_3 retrieved profile

208 concentrations was utilized, which are strongly correlated with ABL values around 900 hPa (~1

209 km) and can represent column average NH_3 concentration from ground to ~1 km. To avoid

210 misunderstanding, we define near surface level in this study as the lowest level of CrIS-derived

211 NH_3 retrieved profile (average from ground to ~1km), and the ground-level as height of 1~1.5

212 m, which is the typical height of site-based observations. As this study focuses on China, we

213 used NH_3 data over regions of 73°-136°E and 3°-54°N and extracted NH_3 concentration within

214 China. To ensure data reliability, only high-quality retrievals were included, filtered using a

215 Quality Flag (QF) $\geq$ 3 and Cloud_Flag = 0. Non-detects (Cloud_Flag = 3) that account for

216 values below the detection limit of the sensor were not included in this study (White et al., 2023;

217 Shephard et al., 2025), but are not expected to have a significant impact in source regions found

218 in China. The analysis period spans from 2013 to 2023, covering both the SNPP and NOAA-

219 20 satellite missions, and provides an 11-year, near-continuous time series of atmospheric NH_3

220 observations over China. To assess the consistency between the two satellite missions, a

221 regression analysis was performed using monthly averaged NH_3 concentrations from the

222 overlapping period (2019-2021), revealing strong agreement and consistency across China

223 (Figure S1, *SI*). For subsequent analyses, the original satellite retrievals were resampled to a

224 uniform spatial resolution of 0.1° × 0.1°.

225

226 **2.2 Ground-based observations of atmospheric NH_3 concentration**

227 The dry deposition of NH_3 is the product of ground-level (usually calculated by site-based

228 observations of 1~1.5 m height) NH_3 concentration and modeled dry deposition velocity. Our

229 previous observation and modeling study in the U.S. Corn Belt found significant vertical

230 gradients within ABL height (~1-2 km) in years of 2017-2019 (Griffis et al., 2019; Hu et al.,

231 2020; 2021). Therefore, the coarse vertical resolution regional satellite mixing ratio values in

232 the lower boundary NH_3 concentration should be converted to better represent local ground

level values at 1~1.5 m, which will further be used to derive NH_3 dry deposition flux. To validate and adjust the regional satellite-derived NH_3 concentrations to better represent surface level sampling observations, we used measurements from the National Nitrogen Deposition Monitoring Network (NNDMN), which was established since 2010 and comprises 43 monitoring sites across China, encompassing different land cover types especially for urban, rural (cropland), and background (coastal, forest, and grassland) regions. The network provides high-quality observations of atmospheric reactive nitrogen (Nr) species in gas, particulate, and precipitation phases, including measurements of both wet and dry nitrogen deposition by using simulated dry deposition velocities (Xu et al., 2015).

NNDMN employs two monitoring methods: the long-term active denuder for long-term atmospheric sampling (DELTA) and the low-cost, passive Active Leading Passive High Absorption (ALPHA) sampler (Flechard et al., 2011). Monthly surface NH_3 concentrations are primarily monitored using DELTA, with a few sites utilizing ALPHA. Xu et al. (2015) demonstrated that these two methods yield statistically consistent NH_3 measurements. The observation periods for most sites range from 2010 to 2015, with detailed site information, including site names, locations, land cover types, and observation periods, provided in Table S1 (*SI*). Given that the satellite data selected for this study spans from 2013 to 2023, the analysis is limited to the period corresponding to the satellite data coverage. For sites where the observation period does not overlap with the satellite research period, and considering the typically low NH_3 concentrations at background sites, this study selected 24 representative urban and rural stations for adjustment to improve the reliability of subsequent NH_3 dry deposition estimates. The locations of monitoring sites and land cover types across China are also shown in Figure. 1a.

As noted above, the calculation of NH_3 dry deposition flux depends on ground-level NH_3 concentrations, although tens of site-based NH_3 concentration observations are available, they cannot provide long term spatial-temporal resolved NH_3 distributions especially in regions with high spatial heterogeneity within China. Therefore, we combined the advantage of ground-

262 based NH$_3$ observations of which can represent heights of 1~1.5 m, and satellite based spatial-

263 temporal NH$_3$ distributions. A linear relationship was constructed by comparing both datasets

264 at the same location and period (Hu et al., 2017; Liu et al., 2024), where the regression equation

265 was used to adjust the lower boundary layer satellite mixing ratio observations to ground-level

266 of 1~1.5 m.

267

268 **2.3 Estimation of NH$_3$ dry deposition**

269 Dry deposition flux of atmospheric NH$_3$ was estimated by multiplying the observed ground-

270 level NH$_3$ concentration with the modeled dry deposition velocity, following the equation:

271 $$F = C \times V_d \qquad (1)$$

272 Here, F denotes the dry deposition flux, C is the ground-level NH$_3$ concentration (ppb) obtained

273 from satellite retrievals and subsequently adjusted using ground-based measurements, and V_d

274 is the dry deposition velocity (cm s^{-1}), which is highly variable in space and time due to its

275 sensitivity to land surface characteristics and meteorological conditions.

276

277 The most widely used approach to derive V_d is by model simulation. Here we first used the

278 GEOS-Chem chemical transport model to simulate spatial-temporal varied V_d across China in

279 2015, with spatial resolution of 0.5° × 0.625° at hourly scale. However, considering (1) the

280 spatial resolution of 0.5° × 0.625° will lead to aggregation errors when quantifying NH$_3$

281 concentration and dry deposition from different land cover types within the same grid cell, and

282 (2) the GEOS-Chem model requires substantial computational resources for one decade, and to

283 further improve spatial resolution and computational efficiency (Figure S2, *SI*), a random forest

284 machine learning algorithm was also applied to simulate dry deposition velocities from 2013 to

285 2023 based on output from GEOS-Chem model (see more details in Section 2.4), where the

286 spatial resolution can improve to 0.25º, see more details in Section 2.4.

287

288 **2.4 Simulation of NH$_3$ dry deposition velocity (V$_d$)**

289 **2.4.1 Simulation of V$_d$ by using GEOS-Chem model**

290 We applied a hybrid modeling approach that combines the GEOS-Chem model with a random

forest regression algorithm to estimate NH_3 dry deposition velocities across China. GEOS-Chem is a global 3-D chemical transport model driven by meteorological inputs from NASA's Goddard Earth Observing System (GEOS), developed for simulating atmospheric composition and chemistry (Eastham et al., 2014). In this study, we used GEOS-Chem v13.3.1 to simulate NH_3 dry deposition velocity over China for the year 2015. The model was driven by assimilated meteorological data from NASA's MERRA-2 reanalysis. Simulations were conducted on a nested horizontal grid of $0.5° \times 0.625°$ covering the domain of 60°E-149.375°E and 11°S-54.5°N (Lu et al., 2024).

2.4.2 Simulation of V_d by using random forest machine learning algorithm

To improve the spatial resolution and model efficiency, we used the GEOS-Chem model based V_d simulations to train a random forest model that can predict dry deposition velocities under various meteorological and land surface conditions and with finer spatial resolution for the entire study period. This data-driven approach enables downscaling to a 0.25° resolution and extends predictions to the entire study period from 2013 to 2023 by using ERA5 reanalysis data.

The random forest (RF) algorithm is a widely adopted ensemble machine learning method that integrates multiple decision trees using the bagging strategy to capture complex nonlinear relationships between predictors and response variables. Overall, the RF model was used for two purposes, (1) for simulating dry deposition velocity (V_d) across 2013-2023, which is displayed in this Section; and (2) to simulate NH_3 concentration and identify key drivers of atmospheric NH_3 changes as illustrated in Section 2.6.1. This RF model has been widely used in atmospheric environment assessments, nitrogen management in agriculture, and model validation studies, providing a robust framework for evaluating the ecological impacts of NH_3 deposition (Asadi et al., 2021; Ai et al., 2024; Zhang et al., 2024). As shown in Figure. S2, the RF model was trained on multiple bootstrapped datasets and evaluated by aggregating outputs from multiple trees to obtain stable and accurate predictions. We selected five meteorological and hydrological variables from ERA5 reanalysis data as predictors: planetary boundary layer height, 10 m wind speed, volumetric soil water of surface layer, surface temperature, and total

320 precipitation. The dataset was randomly split into a training set (60%) and a validation set (40%),

321 the comparisons of V_d simulation by using GEOS-Chem and RF model are evaluated in Section

322 3.4.1.

323

324 **2.5 Geographical division in China and other supporting data**

325 To investigate spatial heterogeneity in interannual trends, China was divided into nine

326 subregions based on the classification system from the Resource and Environmental Science

327 Data Center (Figure 1b). These regions include: Northeast China Plain, Yunnan-Guizhou

328 Plateau, Northern Arid and Semi-Arid Region, Southern China, Sichuan Basin and Surrounding

329 Areas, Middle-Lower Yangtze Plain, Qinghai-Tibet Plateau, Loess Plateau, and Huang-Huai-

330 Hai Plain. Table S2 summarizes the dominant land cover types and their proportional areas

331 within each subregion, and the provinces contained in each region are listed in Table S3 (*SI*),

332 the details of main land cover categories and corresponding proportions in each region are also

333 displayed in Figure 1b and Text S2 (*SI*).

334

335 To clarify the characteristics of atmospheric NH_3 concentrations and dry deposition flux across

336 different land cover types, we utilized the 30-meter resolution China annual Land Cover Dataset

337 (CLCD) to classify surface types. The CLCD is the first annual land cover product for China

338 derived from Landsat imagery, covering the period from 1985 to 2022 (Yang et al., 2021). The

339 dataset categorizes land cover into nine classes: cropland, forest, shrubland, grassland, water

340 bodies, snow/ice, barren land, impervious surfaces, and wetlands. Based on this classification,

341 we conducted a systematic analysis of the spatial variation and temporal trends in NH_3

342 concentrations and dry deposition fluxes across different land surface types.

343

344 In this study, multiple emission inventories of SO_2, NOx, and NH_3 were utilized to investigate

345 the drivers behind changes in atmospheric NH_3 concentrations and to assess potential future

346 trends. The reason of using multiple emission inventories instead of only EDGAR is based on

347 the fact that many previous studies have concluded large potential bias in using a single

348 inventory caused by highly uncertain emission factors and activity data discrepancies (Crippa

et al., 2019; Liu et al., 2024). Therefore, we make full use of all available inventories from different data sources to provide robust evaluation of their emission changes. The emission inventories for SO_2 and NOx include: (1) the Inversed Emission Inventory for Chinese Air Quality (CAQIEI, https://www.scidb.cn/en/detail?dataSetId=81cc0de9c68b4a4981e2f295ac612fbf); (2) the Multi-resolution Emission Inventory for China (MEIC, http://meicmodel.org.cn/?page_id=560); (3) the Air Benefit and Cost and Attainment Assessment System - Emission Inventory (ABaCAS, https://abacas-dss.com/abacasChinese/Default.aspx); (4) the Community Emissions Data System (CEDS, https://github.com/JGCRI/CEDS/); and (5) the Emissions Database for Global Atmospheric Research (EDGAR, https://edgar.jrc.ec.europa.eu/dataset_ap81#p3). Due to the relatively late development of ammonia (NH_3) research and the limited availability of comprehensive emission inventories, this study employed only two datasets—EDGAR v8.1 and MEIC—for NH_3 emission analysis. In addition, the Dynamic Projection model for Emissions in China (DPEC, http://meicmodel.org.cn/?page_id=1917), developed by Tsinghua University, was used to project future emission trends. Further details on all six emission inventories are provided in Text S3 and Table S4-S5 (*SI*). Note the emissions from EDGAR will be used in this study to simulate spatial-temporal patterns of NH_3 concentration. Note the EDGAR does not include biomass burning. However, we also extracted emissions from biomass burning from the MEIC inventory for 2013-2020, the total emissions of SO_2, NO_x, and NH_3 during this period in China, as well as the average annual emissions and their proportions from biomass burning were displayed in Table S6 (*SI*). And the contribution of biomass burning to these three gases was less than 3%, indicating relatively small influence of biomass burning in simulating NH_3 concentrations.

2.6 Quantification of influencing factors to annual trend of NH_3 concentration and dry deposition

2.6.1 Simulation of ground NH_3 concentration by using random forest model

To assess the contributions of meteorological conditions and emissions to NH_3 concentrations

13

378　over the study period, we constructed another RF model to simulate ground-level NH_3

379　concentration. Here the CrIS-retrieved NH_3 concentrations for 2022 were used to train this RF

380　model considering the most updated emission inventory is available for 2022, and input

381　parameters included five ERA5-derived meteorological and hydrological variables (ABL

382　height, wind speed, soil moisture, temperature, and precipitation) and three emission datasets

383　from the EDGAR inventory (SO_2, NO_x, and NH_3 emissions). To isolate the effects of emissions

384　and meteorological variables, we conducted a few sensitivity experiments using the 2022-

385　trained model as the baseline. By holding emissions constant or regressing meteorological data

386　back to 2013 (and vice versa), we simulated NH_3 concentrations attributable solely to changes

387　in meteorology or emissions (for all or each of NH_3, SO_2 and NO_x). The contributions of each

388　factor were then normalized to calculate the percentage influence on NH_3 concentration changes.

389　Note previous modeling results (i.e. $PM_{2.5}$) always suffers from bias in 1/3 of modeling days

390　and it's better to choose days with good predictions. And in this study for NH_3 observations,

391　they were measured by passive sampler, representing averages of one week instead of hourly

392　or daily scales. Therefore, to avoid the random errors from observations and simulations,

393　monthly average was conducted for NH_3 concentration for machine learning.

394

395　**2.6.2 Quantification of influencing factors to annual trends of NH_3 concentration**

396　We further used the logarithmic differentiation method to decompose the relative contributions

397　of NH_3 concentration and dry deposition velocity to the overall change in dry deposition flux.

398　The logarithmic form allows the multiplicative relationship to be transformed into an additive

399　form, making it suitable for quantifying variable impacts, particularly when concentration and

400　velocity change in opposite directions. The decomposition is based on the following:

401　$$\Delta \ln F = \Delta \ln C + \Delta \ln V_d \qquad (2)$$

402　The respective contributions of concentration ($\Delta \ln C$) and deposition velocity ($\Delta \ln V_d$) are

403　calculated as:

404　$$\eta_C = \left| \frac{\Delta \ln C}{\Delta \ln F} \right| \qquad (3)$$

14

$$\eta_{V_{\mathrm{d}}} = \left| \frac{\Delta \ln V_d}{\Delta \ln F} \right| \qquad (4)$$

where Δln denotes the change in the natural logarithm, η_C and η_{Vd} represent relative contributions from NH_3 concentration and dry deposition velocity to dry deposition of F, respectively. These contributions were normalized to provide intuitive percentage values. This method is particularly effective in quantifying dynamic and opposing changes and does not assume linear relationship, offering a more robust analysis than traditional linear regression. Additionally, the Mann-Kendall (MK) trend test was employed to statistically evaluate the temporal trends in NH_3 concentrations over the study period (Text S1, *SI*).

3 Results and Discussions

3.1 Spatial patterns of near surface satellite NH_3 concentration and its trend analysis

Using CrIS satellite-derived near surface NH_3 concentrations (representing average between ground to ~1 km) from 2013 to 2023, a high-resolution (0.1° × 0.1°) monthly averaged NH_3 concentration dataset across China over an 11-year period was generated. The observation from the near surface layer can reflect the impact of human activities and natural source emissions on the near-Earth atmospheric environment. We first displayed the annual averaged spatial patterns and its trend from 2013-2023 at both the national scale and within specific subregions, followed by an analysis of seasonal variations (Figures 2a-j and Figures S3-S7, *SI*). The results of the annual average indicate that the North China Plain (also known as the Huang-Huai-Hai Plain) consistently exhibited the highest NH_3 concentrations (>10 ppb) during the study period (Figure 2a). This region is recognized as one of China's most intensive agricultural zones, accounting for approximately 25% of China's total arable land area and grain production (Song et al., 2024), and is thus subject to frequent fertilizer application, contributing significantly to elevated NH_3 emissions and corresponding concentration.

The secondary NH_3 concentration hotspots were observed in the Guanzhong Plain in Shaanxi Province and the southeastern margin of the Tibetan Plateau. The Guanzhong Plain region is another major agricultural production area in western China, with cultivated land accounting

433 for 49.4% of Shaanxi Province's total arable area. Intensive fertilizer application and related

434 activities are the main sources of NH_3 emissions in this region. The elevated NH_3 concentrations

435 in southeastern Tibet are likely attributed to emissions from extensive livestock farming,

436 particularly yak and sheep husbandry. In addition to these agricultural and pastoral regions,

437 relatively high NH_3 concentrations were also observed in arid zones such as Xinjiang and Inner

438 Mongolia. However, these apparent NH_3 enhancements are likely artifacts of satellite retrievals

439 potentially influenced by surface radiative properties or dust. Higher accuracy is typically

440 associated with higher thermal contrast; conversely, lower thermal contrast would lead to higher

441 uncertainties in NH_3 retrievals, leading to overestimation of NH_3 concentrations due to

442 limitations in retrieval algorithms and thermal contrast biases (Liu et al., 2020b).

443

444 To further explore spatial patterns in temporal change, the pixel-wise trend analysis of annual

445 NH_3 concentrations was also conducted (Figure 2b). Significant positive trends (>0.4 ppb yr^{-1})

446 were found in the central and eastern parts of China, particularly in major agricultural zones

447 with intensive crop fertilization. These results are consistent with findings by Warner et al.

448 (2017), who reported a substantial increase in NH_3 concentrations over eastern China using

449 AIRS data from 2002 to 2016. Our study extends this trend through 2023, indicating that NH_3

450 concentrations in these regions have continued to rise significantly in recent years. In contrast,

451 western China generally showed stable or declining trends. Although northern Xinjiang

452 exhibited moderate NH_3 increases in areas where the trend passed significance testing, other

453 parts of the west demonstrated declining trends. This pattern may be associated with grassland

454 restructuring policies implemented by the Chinese government to reduce overgrazing and

455 restore degraded ecosystems. These measures have significantly alleviated the ecological

456 pressure on grasslands and fostered the transformation and upgrading of grassland animal

457 husbandry, as well as environmental optimization. Therefore, with policy support, they

458 contribute to reducing environmental pollution from animal husbandry in grassland areas,

459 thereby lowering NH_3 emissions.

460

461 The spatial patterns of NH_3 concentration increases correspond closely to regions of high

population density and agricultural land cover types, such as the North China Plain and Sichuan Basin. These areas are also hotspots for reductions in SO_2 and NO_x emissions due to stringent air pollution control measures as displayed in Figures S8-S9 (*SI*). The decline in acid gases may reduce atmospheric neutralization capacity, thereby enhancing the lifetime and apparent abundance of NH_3 in the atmosphere (Dong et al., 2023), contributing to the pronounced upward trends observed in these regions.

We also displayed the seasonal variations and its trend during 2013-2023, clear seasonal differences in NH_3 spatial distribution were observed during the whole study period (Figure 2c-j, Figures S4-S7, *SI*). In spring, the NH_3 distribution resembled the annual pattern but exhibited concentrations approximately 13.9% higher. The Huang-Huai-Hai Plain showed especially concentrated and elevated values, likely due to extensive fertilizer use during spring planting. In contrast, the northwest exhibited little seasonal deviation from annual averages, as emissions are more influenced by pastoral activities than by seasonal patterns of fertilization in agricultural regions. In autumn, NH_3 levels declined sharply, despite localized fertilizer application, primarily due to reduced emissions and cooler temperatures. High concentrations remained in Shandong Province and adjacent regions. Winter concentrations were the lowest, reflecting widespread agricultural dormancy and low temperatures, although lower thermal contrast and reduced NH_3 signal strength increase retrieval uncertainties.

In summer, NH_3 concentrations peaked across China, with higher concentration regions expanding westward into semi-arid areas. This peak seasonality contrasts with trends in Europe and the U.S., where springtime peak is also more typical. In China, summer fertilization is applied for the key agricultural crops as rice paddy, maize, corn and wheat—often involving both mineral and organic fertilizers—contributes to the observed summer peak (Paulot et al., 2014; Luo et al., 2025). Elevated temperatures further enhance volatilization from manure of agricultural area and urban waste in cities, intensifying atmospheric NH_3 concentration. Although urbanization has increased over the past decade, many system-scale farms continue to be used for agricultural production. As reported by Liu S et al. (2024) that temperature

increases accounted for up to 20.0% of urban NH_3 increases between 2008 and 2019. Notably, elevated NH_3 levels were also observed along the Yangtze River basin, corresponding to fertilizer use in rice paddies.

The spatial distributions of the 11-years trend analyses for each season are also displayed (Figures 2d, f, h and j), they show significant increases across eastern China, particularly during summer and autumn. Overall, these results indicate the annual trend of surface NH_3 concentration occurred throughout each season. Winter trends were the weakest in magnitude and spatial extent. Consistent with annual patterns, the North China Plain and Sichuan Basin showed the most pronounced increases. There was no significant change in trend in most parts of western China. There was a slight increasing trend in summer and autumn in northern Xinjiang. Other regions exhibiting a significant trend were decreasing.

3.2 Temporal variation of near surface satellite NH_3 concentrations for different regions

In this section, we continue to present the spatiotemporal near-surface NH_3 concentrations derived from CrIS lower ABL mixing ratio values. The temporal variation of annual NH_3 concentrations and across different seasons from 2013 to 2023 is displayed in Figure 3a. Over this period, the annual mean NH_3 concentration in China increased by 22.5%, with seasonal increases of 13.8% in spring, 30.6% in summer, 26.4% in autumn, and 18.1% in winter, respectively. Among these seasons, summer exhibited the highest mean concentration (3.60 ppb), followed by spring (3.28 ppb), with annual, autumn, and winter means recorded at 2.88 ppb, 2.63 ppb, and 2.00 ppb, respectively (Table 1). The Mann-Kendall trend test results (Table 1) indicated statistically significant upward trends for spring, summer, autumn, and annual mean concentrations ($p < 0.05$). Although winter showed a positive trend ($Z > 0$), it did not reach statistical significance. The seasonal rates of increase, in descending order, were: summer (0.065 ppb yr^{-1}), autumn (0.050 ppb yr^{-1}), annual (0.045 ppb yr^{-1}), spring (0.039 ppb yr^{-1}), and winter (0.023 ppb yr^{-1}). The most pronounced increase during summer from 2013 to 2023 also aligns with previous findings by Liu et al. (2018), which only analyze the North China Plain region from 2008 to 2016. However, their trend is slightly lower than our results, the

520 comparisons reveal a significant increase in NH_3 concentrations after 2016, which could

521 potentially be attributed to enhanced NH_3 emissions, favorable climatic conditions, or a

522 decrease in NOx/SO_2 emissions, as discussed and quantified below.

523

524 The increasing summer trend of atmospheric NH_3 is likely related to global warming in study

525 period (Figure S10, *SI*). The summer temperatures in China rose by 0.3°C from 2013 to 2023.

526 As reported in our previous study on the U.S. Corn Belt, NH_3 emissions are projected to increase

527 by a factor of 2.5 for every 10°C rise in summer temperatures (Hu et al., 2020; 2021). Other

528 studies also showed that over 40% of fertilizer application and approximately 25% of livestock

529 emissions occur during the summer months (Xu et al., 2015; Kang et al., 2016), which enhances

530 NH_3 volatilization from ground to atmosphere. The slower rate of increase in spring may be

531 associated with China's national fertilizer reduction policies, such as the "Action Plan for

532 Fertilizer Reduction by 2025". Fertilizer use increased until peaking in 2015 and subsequently

533 declined for eight consecutive years, resulting in a 15.1% reduction from 2013 to 2023, with

534 the national application totaling 50.22 million tons in 2023 (Figure S11, *SI*).

535

536 The decrease in chemical fertilizer use, combined with the adoption of organic fertilizers, has

537 contributed to a gradual slowdown in the rise of NH_3 concentrations. By 2024, the nitrogen use

538 efficiency (NUE) for rice, maize, and wheat reached 42.6%, helping to reduce fertilizer input

539 without compromising yields and mitigating NH_3 emissions and nutrient pollution. Zhan et al.

540 (2020) identified improving NUE as the most effective and cost-efficient strategy for NH_3

541 mitigation in agriculture, a finding supported by cost-benefit assessments. Autumn also showed

542 a substantial increase in NH_3 concentrations, second only to summer. Current emission

543 reduction efforts have primarily focused on spring and summer, reflecting crop planting cycles,

544 while autumn has often been overlooked, contributing to this seasonal gap in mitigation. These

545 findings highlight the need for seasonally and crop-specific emission control strategies in future

546 NH_3 management efforts.

547

548 Significant spatial heterogeneity was observed in the interannual variation of NH_3

concentrations across different regions. Figure 3b illustrates long-term trends in NH_3 concentrations for nine subregions. Most regions exhibited increasing trends, with the Huang-Huai-Hai Plain standing out for its consistently elevated concentrations—approximately twice as high as the national average (Table 2). This region is China's primary agricultural zone, characterized by high population density and intensive agricultural activity, both of which contribute to substantial NH_3 emissions. Additionally, it has been a focal area for SO_2 and NO_x emission reductions, and the combined effects of high emissions and reduced atmospheric neutralization capacity have led to persistent NH_3 accumulation.

The trend analysis further revealed statistically significant upward trends in the Huang-Huai-Hai Plain, the Northern Arid and Semi-Arid Region, the Loess Plateau, the Middle-Lower Yangtze Plain, South China, the Northeast China Plain, and the Sichuan Basin and its surrounding regions. We used compound annual growth rate (CAGR) method to calculate the annual growth rate of NH_3 concentration across the country and in the Huang-Huai-Hai Plain region. The Huang-Huai-Hai Plain showed the steepest increase, with an average annual rise of 0.24 ppb, corresponding to a 6.0% per year growth rate—3 times the national average of 2.0% (Manisha et al., 2025). The primary driver of this sharp increase is the marked reduction in atmospheric SO_2, which has disrupted the NH_3-acid gas neutralization balance (Xu et al., 2019a). The Loess Plateau ranked second, with an average increase of 0.14 ppb per year. In contrast, the Yunnan-Guizhou Plateau exhibited a mild, non-significant increase, with relatively stable concentrations. The Tibetan Plateau showed a slight downward trend, which also lacked statistical significance ($p > 0.05$), indicating a relatively stable NH_3 regime in this high-altitude, low-emission region.

3.3 Comparison between satellite and ground-based NH_3 observations and adjustment from surface level to ground-level NH_3 concentration

As stated in Section 2.1, although satellite-based observations provide extensive spatial coverage and long-term data for atmospheric NH_3 studies, they have limited vertical profile resolution of mixing ratio values near the surface that often cannot capture the reported fine

578   scale vertical gradient in the lower ABL created from the reactive nature of ammonia and its

579   role in chemical transformation processes (Hu et al., 2020; 2021; Griffis et al., 2019). Further,

580   the dry deposition of NH_3 is the product of ground-level (usually calculated by site-based

581   observations of 1~1.5 m height) NH_3 concentration and dry deposition velocity. Therefore, to

582   enable accurate estimation of NH_3 dry deposition, we conducted a comparative analysis

583   between satellite-derived and multiple years of observations at 24 ground-based NH_3 sites, and

584   their relationship will be used to adjust the lower vertical resolution satellite observations to

585   ground-based surface observations.

586

587   As shown in Figure 4a, the scatter plots of monthly averaged site-based ground-level NH_3

588   concentrations and corresponding satellite-based observations exhibit a strong correlation with

589   a coefficient of determination (R^2) of 0.62 and a root mean square error (RMSE) of 3.56 ppb.

590   Note, to minimize the random error, each plot in Figure 4a represents averages of all

591   observations at urban or rural sites during each overlap month. Overall, it illustrates that the

592   ground-level measurements are, on average, approximately twice as high as those retrieved by

593   satellite. This discrepancy can be attributed to the vertical gradient of NH_3 in the atmosphere:

594   ground-based sensors typically local point source observations operate at heights of 1-1.5 m,

595   while satellite observations are regional (14 km) with low vertical resolution (~1km or more),

596   which is shown from the averaging kernels (Shephard et al.,2011, Shephard et al., 2020). Many

597   pioneer studies have demonstrated that when the land surface acts as an NH_3 source, its vertical

598   distribution decreases logarithmically with height (Hu et al., 2020; 2021; Shephard et al., 2011;

599   Shephard et al., 2020). For example, our previous studies of tall tower observations in the

600   United States reported an NH_3 mixing ratio gradient of -0.27 ppb per 100 m, with modeled

601   gradients ranging from -0.21 to -0.84 ppb per 100 m (Hu et al., 2020; 2021; Griffis et al., 2019),

602   showing good agreement between observations and simulations of the vertical profiles within

603   boundary layer. When using the gradient of above reported values, the average of 0-1000 m

604   column NH_3 concentration should be around 1~ 4 ppb lower than ground-level, this pronounced

605   vertical gradient is a major reason for the systematic underestimation of NH_3 by satellites when

606   compared with ground-level observations.

607   To address this inconsistency, we used the regression relationship derived from Figure 4a to

608   adjust the satellite retrievals. After correction, a new regression (Figure 4b) shows a nearly 1:1

609   agreement between satellite and ground-based measurements, with the RMSE reduced from

610   3.56 ppb to 1.69 ppb. The purpose of the linear regression equation is to adjust the column-

611   averaged NH_3 concentration to the ground-level at 1.5 m, as described in Section 2.2. The

612   approach we used is applying an additive shift (bias correction), where R^2 remain almost the

613   same (Figures 4a-b), it's also based on "K-theory" (gradient diffusion theory) with the well-

614   mixed assumption in the ABL. This method assumes that transport flux can be represented

615   analogously to molecular diffusion, where fluxes are proportional to the mean gradient of the

616   transported quantity. This adjustment enables the derivation of NH_3 dry deposition, which can

617   then be compared with global observations. The reason that the R^2 value remained unchanged

618   is that the same equation, y=0.35+0.16, was applied to all scatter plots. This theoretically affects

619   only the RMSE and does not influence the R^2 value. The reduction in RMSE further indicates

620   that this approach effectively adjusts the column-averaged NH_3 concentration to the ground-

621   level at 1.5 m. The conversion is given by x=(y-0.16)/0.45=2.22y-0.36 , where y represents the

622   CrIS satellite-based column-averaged NH_3 concentration (from ground to 1 km), and x denotes

623   the NH_3 concentration after adjustment to 1.5 m. This approach is conceptually similar to using

624   a simple multiplicative (or additive) conversion factor. It is important to acknowledge that

625   spatial-temporal uncertainties or potential systematic biases may exist in the relationship

626   between ground-based and satellite-derived NH_3 observations across different regions and

627   under varying thermal contrast and boundary-layer conditions. As demonstrated in the scatter

628   plots of Figure 4a-b, which exhibit significant variability. Nevertheless, the regression slope

629   and associated uncertainty were 0.45 ± 0.04, indicating that the potential systematic biases

630   mentioned above could result in an error of approximately 9% when deriving ground-level NH_3

631   concentrations and dry deposition rates. This error was calculated by dividing the uncertainty

632   extent (0.04) by the regression slope (0.45). These uncertainties can be mitigated by increasing

633   the number of ground-based NH_3 observations in diverse regions in future studies.

634

635   To further assess the adjustment effectiveness, we selected the year 2015—when both satellite

636 and ground data are available—for analysis. As shown in Figure 4c, the adjusted satellite-based

637 NH$_3$ concentrations closely match ground observations across almost all sites, confirming the

638 reliability of using the adjustment approach. This adjustment function was then applied to the

639 full 2013-2023 satellite dataset to improve the reliability of NH$_3$ dry deposition estimates. Table

640 2 illustrated the adjusted average of ground-level NH$_3$ concentrations across different regions,

641 with the Huang-Huai-Hai Plain exhibiting the highest value of 11.36 ppb. This was followed

642 by the Northern Arid and Semi-Arid Region (6.93 ppb), the Qinghai-Tibet Plateau (6.48 ppb),

643 and the Loess Plateau (6.05 ppb). Although the height-corrected NH$_3$ concentrations in these

644 regions ranked immediately after the Huang-Huai-Hai Plain, their values were approximately

645 two times lower than those observed in the Huang-Huai-Hai Plain.

646

647 **3.4 Estimation of spatiotemporal variations of NH$_3$ dry deposition across China**

648 **3.4.1 Simulation of spatiotemporal dry deposition velocities**

649 As illustrated in Method Section 2.4, to estimate NH$_3$ dry deposition flux across China, we first

650 used the GEOS-Chem model to simulate NH$_3$ dry deposition velocities for the year 2015

651 (Figure 5a). Considering the high computational cost, limited temporal flexibility and spatial

652 resolution of the GEOS-Chem model, we adopted a hybrid modeling approach by training a

653 random forest (RF) machine learning model on the GEOS-Chem model-based simulation

654 results. This approach allowed us to extend the simulation to the full 2013-2023 period, while

655 improving both computational efficiency and spatial resolution from 0.5° × 0.625° to 0.25° ×

656 0.25°.

657

658 The resulting RF-predicted dry deposition velocities for 2015 show high spatial agreement with

659 the GEOS-Chem outputs (Figure 5b and Figure S12, *SI*). Both models identify southern China

660 as a hotspot for dry deposition velocity, likely due to the region's warm and humid conditions

661 that facilitate gaseous NH$_3$ deposited onto ground surface. Additionally, southern China is a

662 major rice-producing region where surface resistance in paddy fields is lower than in dryland

663 fields, further enhancing dry deposition rates. Figure 5c shows the differences between the two

664 model outputs, with over 99% of grid cells having discrepancies less than 0.1 cm s^{-1}, indicating

665 strong consistency and validating the reliability of the RF model for long-term simulations.

666 Using this trained model, we further simulated NH_3 dry deposition velocities from 2013 to 2023

667 at monthly averages.

668

669 **3.4.2 The spatiotemporal variations of NH_3 dry deposition in China**

670 With the adjusted spatiotemporal ground-level NH_3 concentrations and simulated deposition

671 velocities from 2013 to 2023, we derived the monthly grid-level NH_3 dry deposition flux for

672 China. These were further aggregated to estimate average NH_3 dry deposition flux and total

673 deposition over different land cover types (Figure 6; Figure S13, *SI*). Figure 6a illustrates the

674 spatial distribution of NH_3 dry deposition flux average from 2013 to 2023. Distinct spatial

675 differences are evident, where the eastern coastal regions exhibited significantly higher

676 deposition flux than inland areas, with values higher than 1.8 g NH_3 m^{-2} yr^{-1}. Notably, the

677 Huang-Huai-Hai Plain and the southwestern region of the Qinghai-Tibet Plateau emerged as

678 prominent hotspots of NH_3 dry deposition, highlighting the substantial impact of intensive

679 agricultural activities and industrial emissions. Elevated deposition rates were also observed in

680 the southern Tibetan Plateau, driven by locally high NH_3 concentrations.

681

682 A trend analysis of dry deposition over the 11-year period (Figure 6b) shows statistically

683 significant increases in deposition flux in eastern coastal areas (> 0.1 g m^{-2} yr^{-1}), likely

684 reflecting rising NH_3 concentrations in these regions. In contrast, western China shows minimal

685 change, with some areas even exhibiting slight declines. Unlike the NH_3 concentration trends,

686 there is no region in western China that displayed a statistically significant increase in dry

687 deposition flux, which was caused by the trend of V_d in this region, emphasizing the spatial

688 decoupling between emission intensity and deposition patterns in less industrialized regions.

689

690 The interannual variation of NH_3 dry deposition also exhibited significant spatial heterogeneity

691 at the regional scale (Figure 6c and Table 3). The Huang-Huai-Hai Plain, characterized by

692 persistently high NH_3 concentrations, recorded the highest area-specific dry deposition flux,

693 reaching 1.06 g m^{-2} yr^{-1}—approximately twice the levels observed in other regions. MK trend

694   analysis indicated a significant increasing trend in dry deposition flux across all regions except

695   the Tibetan Plateau, where a weak downward trend was observed but was not statistically

696   significant. The most pronounced increase was found in the Huang-Huai-Hai Plain, with an

697   average annual increment of 0.05 g m^{-2} yr^{-1}, followed by the middle and lower reaches of the

698   Yangtze River, at 0.03 g m^{-2} yr^{-1}, detailed numbers are displayed in Table 3.

699

700   **3.4.3 Comparisons of ground-level NH$_3$ concentration, dry deposition velocity and flux in**

701   **different land cover types**

702   In addition to meteorological factors, land cover types play a pivotal role in regulating dry

703   deposition processes. In this section, we annually extracted and compared ground-level NH$_3$

704   concentrations, dry deposition velocities, and dry deposition fluxes across different land cover

705   categories. The analysis focused on four representative land-use types—urban, cropland, forest,

706   and grassland—selected based on their distinct NH$_3$ emission characteristics (Figure 7; Table

707   S7, *SI*). The average NH$_3$ concentrations, ranked from highest to lowest, were: urban (8.76 ppb),

708   cropland (6.27 ppb), national average (6.01 ppb), grassland (5.72 ppb), and forest (3.76 ppb)

709   (Figure 7a). Urban areas exhibited both the highest concentrations and the largest interannual

710   variability, with a statistically significant upward trend ($p < 0.05$, $Z > 1.96$), increasing at an

711   average rate of 0.39 ppb yr^{-1}. This trend is primarily attributed to anthropogenic sources such

712   as vehicular emissions, as well as the urban heat island effect, which raises urban temperatures

713   by 1-3°C—and occasionally by over 10°C—relative to surrounding rural areas (Santamouris et

714   al., 2013; Cao et al., 2016; Chang et al., 2021). These elevated temperatures, further amplified

715   by global warming, facilitate enhanced NH$_3$ volatilization within cities.

716

717   While ground-level NH$_3$ concentrations over grassland areas remained relatively stable

718   throughout the study period, cropland regions exhibited a continuous upward trend, with the

719   two trends intersecting in 2016 (Figure 7a), after which NH$_3$ concentrations in croplands

720   exceeded those in grasslands. NH$_3$ emissions in grassland ecosystems are predominantly

721   associated with livestock grazing, and the stabilization observed is likely attributable to the

722   implementation of grazing restrictions and ecological restoration policies. In contrast, despite

the introduction of fertilizer reduction policies in some agricultural areas, rising food demand driven by population growth has sustained or even increased fertilizer application, thereby contributing to the observed increase in cropland NH_3 concentrations. At the national scale, NH_3 concentrations exhibited a statistically significant upward trend, with an average increase of 0.10 ppb yr^{-1} (equivalent to an annual growth rate of 2.2%). Forested regions, which are minimally impacted by anthropogenic sources such as synthetic fertilizers and livestock emissions, maintained the lowest and most stable NH_3 concentrations, showing only a slight upward trend that may be linked to climate warming (Figure 7a; Figure 8).

Dry deposition velocities exhibited limited interannual variability across different land cover types. Forested areas recorded the highest average deposition velocity, likely attributable to greater surface roughness and enhanced canopy-induced turbulence, followed by urban and cropland regions (Figure 7b; Figure 8). The mean NH_3 dry deposition velocities for forest, urban, cropland, grassland, and the national average were 0.43, 0.42, 0.40, 0.32, and 0.36 cm s^{-1}, respectively. Mann-Kendall trend analysis revealed statistically significant increasing trends in urban and cropland areas, with annual rates of 0.0013 and 0.0012 cm s^{-1} yr^{-1}, respectively. Although forests maintained the highest mean velocity and exhibited a positive trend, the change was not statistically significant. At the national scale, deposition velocity showed a weak but consistent upward trend. In contrast, grassland areas experienced a slight decline in deposition velocity over the 11-year period, though this trend was not statistically significant.

Area-specific NH_3 dry deposition fluxes closely followed the spatial distribution of atmospheric concentrations across different land cover types (Figure 7c; Figure 8). Urban regions exhibited the highest deposition flux (0.88 g m^{-2} yr^{-1}), followed by cropland areas (0.61 g m^{-2} yr^{-1}). Both urban and national average fluxes demonstrated statistically significant upward trends over the study period. The steepest increase was observed in urban areas, with a rate of 0.04 g m^{-2} yr^{-1}— approximately four times the national average—followed by croplands at 0.03 g m^{-2} yr^{-1}. Our findings also agree the previous study by Chen P et al. (2023), which conducted that, although fertilizer application has been partially reduced under agricultural emission control policies,

non-agricultural sources—such as industrial processes and transportation—have become the predominant contributors to NH_3 emissions in China, particularly concentrated in urban areas. This shift has contributed to elevated NH_3 concentrations and enhanced dry deposition fluxes in cities.

In contrast, forests and grasslands showed relatively stable fluxes, likely due to lower levels of anthropogenic disturbance. Nevertheless, a statistically significant increasing trend in forest deposition flux was detected, which may have important ecological implications. Sustained increases in NH_3 deposition could lead to adverse effects such as plant nutrient imbalances, biodiversity loss, and eutrophication of adjacent aquatic systems, potentially compromising forest health and long-term ecosystem stability. Furthermore, interannual variability in dry deposition was more pronounced in urban areas, reflecting the dynamic nature of urban development and emission variability, whereas cropland fluxes exhibited a more gradual trend in response to evolving fertilizer management practices.

Trends in total NH_3 dry deposition across different land cover types generally mirrored those of area-specific fluxes; however, total dry deposition values of NH_3 were modulated by the area of each land cover type. Grasslands accounted for the largest share of annual total NH_3 dry deposition (1.23 Tg), followed by croplands (1.15 Tg), forests (0.92 Tg), urban areas (0.21 Tg), and a national total of 4.85 Tg. Over the 11-year study period, statistically significant upward trends in total dry deposition were observed at the national scale, as well as in cropland, forest, and urban areas, with annual increases of 0.10, 0.05, 0.03, and 0.01 Tg yr^{-1}, respectively. Although grasslands also exhibited an increasing trend, it was not statistically significant. Changes in annual total NH_3 dry deposition are driven not only by atmospheric concentrations and deposition velocities but also by land-use dynamics (Figure 7d; Figure 8). In particular, the continuous expansion of urban areas from 2013 to 2023 contributed substantially to the increasing trend in total urban NH_3 deposition (Figure S14, *SI*). These findings highlight the importance of considering both biogeochemical processes and anthropogenic land-use changes in assessing long-term trends in reactive nitrogen deposition.

3.5 Simulation of ground-level NH₃ concentration and contribution factors analysis to both NH₃ concentration and deposition flux

In this section, we quantified and partitioning the contributions influencing the trends in the NH_3 concentration and dry deposition flux, and further investigated the key drivers of atmospheric NH_3 concentrations using the Random Forest (RF) regression model. Model performance was evaluated by comparing simulated NH_3 concentrations with observations for the period 2013-2023, showing good agreement (Figure 9). The RF model effectively captured the spatial variability of NH_3 concentrations, with deviations generally within ±0.1 ppb, indicating robust predictive capability. The input variables were categorized into two major groups: meteorological factors and anthropogenic emissions, including NH_3 emissions as well as SO_2 and NOx emissions. The feature-importance ranking figure illustrates the relative importance of eight driving factors in predicting NH_3 concentrations using the Random Forest model (Figure S15, *SI*). Among the emission and meteorological-hydrological factors, the latter plays a more prominent role in explaining the spatial and temporal variability of NH_3 concentrations. Within the meteorological-hydrological factors, the 10-meter wind speed (20.3%), 2-meter temperature (14.9%), and boundary layer height (13.1%) are the most influential variables affecting the NH_3 concentration simulation. These variables collectively reflect the role of atmospheric diffusion capacity and volatilization conditions in regulating the distribution of NH_3 concentrations. Total precipitation (11.0%) and surface soil moisture content (13.6%) contribute to the removal of NH_3 from the atmosphere, though their relative importance is lower. Among the emission factors, NH_3 emissions (16.4%) are the most significant, followed by NO_x (11.0%) and SO_2 (5.1%) emissions. This suggests that, in addition to direct emissions, precursor chemical processes also have an indirect influence on the distribution of NH_3 concentrations.

To quantify the contribution of emissions and meteorological factors to changes in NH_3 concentrations, we used a random forest model to simulate NH_3 concentration with different sensitivity test by replacing single factor, and the difference between them can be treated as contributions from corresponding factor. Figure 10a shows the adjusted ground-level NH_3

concentration in 2022 and the simulation results under three different meteorological and emission scenarios. The simulated concentrations are 3.08 ppb, 3.14 ppb, 3.10 ppb. Both meteorological and emission contributions are calculated from the simulation results. Simulation results from the random forest model showed that anthropogenic emissions were the main driver, accounting for approximately 77.4% of the NH_3 concentration changes, while meteorological conditions accounted for the remaining 22.6% (Figure 10a).

The above relative contributions are calculated by the method that using the emissions and meteorological-hydrological factors from 2013 as the baseline (more details in Method Section 2.6.1), we first simulated the NH_3 concentration for 2022 using the emissions and meteorological-hydrological factors from that year. The simulated concentration was 3.08 ppb, which was consistent with the satellite-observed concentration for 2022, yielding a relative error of 0.1%. Subsequently, we replaced the emissions data with those from 2013 while keeping the 2022 meteorological-hydrological factors constant, resulting in a simulated concentration of 3.14 ppb. We then replaced the meteorological-hydrological factors with those from 2013 while keeping the 2022 emissions constant, leading to a simulated concentration of 3.10 ppb. By subtracting the two simulated concentrations from the 2022 NH_3 concentration simulation, we quantified the effects of changes in emissions and meteorological-hydrological factors on NH_3 concentration. Finally, the results were normalized, revealing that the relative contributions of emissions and meteorological-hydrological factors to the concentration changes were 77.4% and 22.6%, respectively.

Among meteorological parameters, air temperature emerged as the most influential factor, whereas other variables (e.g., relative humidity, wind speed) exhibited minimal interannual variation and lower predictive importance. Analysis of ERA5 reanalysis data revealed a persistent warming trend over the past decade, with the annual mean surface temperature in 2023 being 8.4% higher than in 2013 (Figure S10, *SI*). Previous studies, such as Hu et al. (2020), reported an exponential relationship between NH_3 mixing ratios and temperature, with NH_3 concentrations increasing from 4 ppb to 19 ppb as temperature increased from 0°C to 10°C.

839   The regional temperature sensitivity (Q_{10}) of NH_3 emissions was estimated to be approximately

840   2.5, indicating that continued warming will likely enhance NH_3 volatilization. This may further

841   exacerbate nitrogen loss from agricultural systems and elevate NH_3 dry deposition to downwind

842   natural ecosystems, potentially intensifying ecological risks such as eutrophication and

843   biodiversity loss.

844

845   Figure S16 (*SI*) illustrates multi-year emission trends of SO_2, NOx, and NH_3 derived from

846   multiple emission inventories, including EDGAR and MEIC; considering the potential

847   uncertainty of pollution emission inventories, the comparisons of different inventories can

848   provide robust results of emission trends. Although observed atmospheric NH_3 concentrations

849   have increased over the period 2013-2023, all inventories consistently indicate a slight decline

850   in NH_3 emissions. This apparent contradiction suggests that the observed rise in NH_3

851   concentrations may be primarily driven by reduced emissions of acidifying species—namely

852   SO_2 and NOx—which typically enhance NH_3 partitioning into the particulate phase. The

853   reductions in SO_2 and NOx emissions may have suppressed their atmospheric reactions with

854   NH_3, thereby decreasing the formation of particulate ammonium and leaving a greater fraction

855   of NH_3 un-neutralized in the gas phase. This shift likely contributed to elevated ambient NH_3

856   concentrations, as reported in previous studies (Xu et al., 2019a; Liu et al., 2018; Liu et al.,

857   2017a).

858

859   We also investigated the temporal changes of agricultural fertilizer application and livestock

860   farming in China from 2013 to 2023, which are treated as the dominating source of NH_3

861   emissions in China (Figures S17-S18, *SI*). During the study period, the application rate of

862   agricultural fertilizers in China showed a trend of first increasing and then decreasing, reaching

863   a peak in 2015, and then continuing to decline until 2023. In order to reveal the changing

864   characteristics of different regions more clearly, we examined the change of agricultural

865   fertilizer amount in each region, and the results indicated that all regions showed a downward

866   trend. At the same time, the total amount of livestock breeding in China first decreased and then

867   rose during the same period.

868   Furthermore, it is important to note that, although satellite based observations from 2013 to
869   2023 reveal a clear upward trend in NH_3 concentrations at both column-averaged near surface
870   level and ground-level, emission inventories from EDGAR, MEIC, and previous bottom-up
871   estimates suggest that NH_3 emissions in China have stabilized or declined gradually in recent
872   years (Liao et al., 2022; Zheng et al., 2018). This discrepancy is not only evident in the current
873   study but has also been observed in other research, where some satellite-based NH_3 inversion
874   studies show varying degrees of increasing trends (Zhang et al., 2017; Evangeliou et al., 2021;
875   Luo et al., 2022). The difference may stem from the inherent contrasts between "bottom-up"
876   and "top-down" estimation methods as displayed in Figure 13c. Several top-down studies
877   indicate that the observed rise in NH_3 emissions could be partially explained by the neglect of
878   SO_2 and NOx column concentration changes. For instance, Luo (2022) estimated global NH_3
879   emissions from 2008 to 2018 using a top-down approach and found that NH_3 emissions in
880   eastern China increased by 61% per decade (6.6 Tg a^{-1} per decade), particularly after 2013,
881   driven primarily by the rise in IASI NH_3 column concentrations. However, when the model
882   incorporated the decreasing SO_2 and NOx column concentrations, NH_3 emissions in eastern
883   China were found to decrease by 19% per decade, with the decline becoming more pronounced
884   after 2013 (28% per decade), aligning more closely with inventory results. This suggests that
885   SO_2 and NOx concentrations play a significant role in mitigating atmospheric NH_3 levels.
886   Additionally, both SO_2 and NOx emissions are negatively correlated with NH_3 concentrations
887   to some extent (Deng et al., 2022). In summary, there are large differences in the estimation of
888   NH_3 emissions by different methods, so it is necessary to further strengthen the comprehensive
889   analysis and mutual verification of various methods (such as emission factor method, satellite
890   observation inversion method and field observation method) to improve the accuracy and
891   reliability of estimation results (Chen P et al., 2023).

892   According to EDGAR data, national SO_2 and NOx emissions declined by approximately 20.0%
893   from 2013 to 2022, following the implementation of the Air Pollution Prevention and Control
894   Action Plan in 2013, which led to substantial reductions in these precursor gases. It is important
895   to note that our Random Forest model does not account for atmospheric chemical processes
896   involving the formation and partitioning of secondary inorganic aerosols, such as nitrate (NO_3^-),

897　　sulfate (SO_4^{2-}), and ammonium (NH_4^+). Therefore, for future investigations aiming to quantify

898　　the role of atmospheric chemistry in modulating NH_3 concentrations and deposition, the use of

899　　comprehensive atmospheric chemical transport models such as WRF-Chem or GEOS-Chem is

900　　strongly recommended. These models are capable of resolving multiphase chemical reactions

901　　and the thermodynamic partitioning of NH_3 into the aerosol phase, thereby offering a more

902　　mechanistic understanding of NH_3 dynamics in response to co-emitted precursor changes.

903

904　　To further elucidate the drivers of NH_3 dry deposition trends, we employed the method

905　　described in Section 2.6.2 to decompose the relative contributions of changes in NH_3

906　　concentrations and deposition velocities across different land cover types (Figure 10b; Table

907　　S8, *SI*). All variables were normalized to facilitate comparison of relative contributions. The

908　　results show that the change of NH_3 dry deposition was mainly driven by the change of

909　　atmospheric NH_3 concentration, which accounted for 72.6%-81.2% of the total contribution in

910　　China and four land cover types. Among them, the concentration changes in urban areas

911　　contributed the least (72.6%), and the dry deposition rate change contributed the most (27.4%),

912　　likely reflecting the more complex aerodynamic and surface resistance conditions in urban

913　　environments. In contrast, forested areas showed the highest concentration-driven contribution

914　　(81.2%), consistent with their relatively stable surface characteristics and low anthropogenic

915　　disturbance.

916　　To quantify the individual contribution from SO_2 and NO_x, we also applied the constructed RF

917　　model with the method introduced in Section 2.6.1. Taking 2013 as the benchmark, the SO_2 and

918　　NO_x emissions in 2022 are simulated back to the level of 2013, and the results are normalized

919　　to calculate the relative contribution. The results show that the contribution of SO_2 is 27.1%

920　　and that of NO_x is 72.9%. The contribution of NO_x is significantly higher than that of SO_2,

921　　which is closely related to the earlier start of SO_2 emission reduction. Long-term SO_2 emission

922　　reduction has changed the composition of acid gases in the atmosphere, causing the relative

923　　concentration of NO_x to rise, gradually becoming the main acid gas reacting with NH_3 (Liu S

924　　et al., 2024).

925   Considering the neutralization effect of SO_2 and NO_x acid gases on NH_3, we analyzed the

926   changes of the three emissions (Table S9, *SI*). The data in Table S9 shows that the relative

927   annual reduction rates and total reduction rates of the three are similar, with values around 2.5%

928   and 20.5%. However, in terms of the average annual reduction, the reduction scale of SO_2 is

929   about 3 times that of NH_3, and that of NO_x is about 2.4 times that of NH_3. Since the reduction

930   of SO_2 and NO_x is larger, more NH_3 is distributed in the free state in the atmosphere. In addition,

931   SO_2 and NO_x, as acid gases, can react with NH_3 in the atmosphere, and they have a synergistic

932   effect in consuming NH_3. Therefore, although the relative annual reduction rates of the three

933   are similar, the contribution of acid gas as a whole to emission reduction is more significant.

934   From the perspective of chemical reaction measurement relationship, the equation for the

935   reaction between SO_2 and NH_3 to generate ammonium sulfate is: $2SO_2 + 4NH_3 + 2H_2O + O_2$

936    $\rightarrow 2 (NH_4)_2SO_4$. In this reaction, 1 molecule of SO_2 can consume 2 molecules of NH_3; The

937   equation for the reaction between NO_x and NH_3 to generate ammonium nitrate is: $NH_3 + HNO_3$

938    $\rightleftharpoons NH_4NO_3$. This reaction is a 1: 1 measurement relationship and is a reversible reaction. It will

939   re-decompose and release NH_3 under higher temperature or lower concentration conditions.

940   With the intensification of global warming, NH_4NO_3 in the atmosphere will also decompose

941   and release NH_3. Therefore, although the emissions of SO_2, NO_x and NH_3 have all decreased

942   by about 20.5% from 2013 to 2025, the massive emission reduction of SO_2 and NO_x has

943   weakened the consumption capacity of NH_3, resulting in a relative surplus of NH_3 that should

944   have been neutralized, causing NH_3 in the atmosphere. The concentration continues to rise, and

945   the increase of NH_3 concentration also promotes the increase of NH_3 dry deposition.

946   In summary, the observed increase in atmospheric NH_3 concentrations across China is largely

947   attributable to the substantial reductions in SO_2 and NOx emissions. Concurrently, changes in

948   NH_3 dry deposition fluxes are primarily driven by rising NH_3 concentrations, which are

949   indirectly influenced by declining SO_2 and NOx emissions. This inference is supported by

950   consistent evidence from both satellite and ground-based monitoring networks, which

951   document a marked decrease in SO_2 concentrations (Liu M. et al., 2019; Xi et al., 2021),

952   alongside improvements in acid rain conditions.

953

Previous studies have indicated that optimizing fertilizer application and adjusting protein content in animal feed could potentially reduce NH_3 emissions by up to 30% without compromising agricultural yields or incurring additional costs (Zhang et al., 2020). In contrast, regulation of NH_3 emissions has lagged behind that of other pollutants. It was not until the implementation of the 2018 "Three-Year Action Plan for Winning the Blue-Sky Defense Battle" that agricultural NH_3 emissions were formally addressed. This plan emphasized enhanced recycling of livestock waste and measures to reduce NH_3 volatilization. Subsequently, the "14th Five-Year Plan for Energy Conservation and Emission Reduction" further targeted improvements in fertilizer and pesticide use efficiency, setting a goal to reduce NH_3 emissions from large-scale livestock operations in the Beijing-Tianjin-Hebei region by 5%. Although these recent policies have initiated efforts to mitigate NH_3 emissions, the rate of reduction remains substantially lower than that achieved for SO_2.

966

Furthermore, in the context of future warming, we analyzed projected emissions of SO_2, NOx, and NH_3 under five SSP scenarios based on the Dynamic Projection Emission Coefficient (DPEC) inventory developed by Tsinghua University (Figure S19, *SI*). All scenarios indicate declining trends for these pollutants; however, NH_3 exhibits the smallest reduction, amounting to roughly two-thirds of the decreases projected for SO_2 and NOx. This discrepancy, combined with rising temperatures and decreasing acid gas emissions, is expected to further enhance atmospheric NH_3 concentrations. Consequently, despite ongoing mitigation efforts targeting NH_3 emissions, the atmospheric NH_3 concentration may continue to increase. To counteract the synergistic effects of warming and reductions in acid-neutralizing pollutants, more stringent NH_3 emission control policies will be required in China over the coming decades to effectively stabilize or reduce atmospheric NH_3 concentrations.

978

4 Comparison with previous studies and implications

To evaluate and contextualize atmospheric NH_3 concentrations and dry deposition in China relative to other global regions and different land cover types, we conducted a comprehensive

982   literature review summarized in Table 4. This table integrates the findings of the present study

983   with previous assessments of atmospheric NH_3 levels and dry deposition fluxes worldwide. The

984   comparative analysis highlights considerable spatial variability, with NH_3 concentrations

985   ranging from approximately 2 to 10 ppb and area-specific dry deposition fluxes spanning 0.06

986   to 1.00 g m^{-2} yr^{-1}. The values reported in this study are generally consistent with those

987   documented in comparable geographic and climatic regions.

988

989   This study estimates the national average NH_3 concentration in China at 4.98 ppb and the

990   corresponding dry deposition flux at 0.51 g m^{-2} yr^{-1}, and the results for each province of China

991   were also displayed in Figure S20 (*SI*). The national average results closely align with those of

992   Liu et al. (2020a), who employed IASI satellite retrievals and reported NH_3 concentrations of

993   4.15 ppb and dry deposition fluxes of 0.58 g m^{-2} yr^{-1}. The Tianjin megacity, Shandong province,

994   Henan province, Hebei province and Beijing megacity ranked as the largest top 5 regions for

995   NH_3 concentration and dry deposition flux, where Tianjin and Beijing are located within North

996   China Plain hotspots, and were largely influenced by atmospheric transport process from nearby

997   agricultural fields. Compared to Liu et al. (2020a), our analysis extends the observation period

998   and incorporates adjustments against ground-based monitoring data, thereby achieving higher

999   accuracy. Jia et al. (2016) estimated the global NH_3 dry deposition flux using empirical models

1000 based on ground station measurements, reporting a value of 0.68 g m^{-2} yr^{-1} for China.

1001

1002 In contrast, Xu et al. (2015), utilizing averages from 43 ground stations (including 10 urban

1003 stations, 22 rural stations and 11 background stations) from the National Nitrogen Deposition

1004 Monitoring Network (NNDMN), reported substantially higher values for China (10.65 ppb and

1005 1.00 g m^{-2} yr^{-1}) than our study of spatial coverage of whole China. It can be explained by the

1006 representation bias due to the predominance of monitoring sites in urban and rural (mostly

1007 agriculture dominated) regions characterized by elevated NH_3 emissions and

1008 underrepresentation of background locations, resulting in overestimation of national averages

1009 when averaging these observation sites. Further evidence of spatial variability is provided by

1010 Hu et al. (2020, 2021), who documented significant differences in NH_3 concentrations and

1011 deposition rates between cropland and forested background sites, underscoring the critical

1012 influence of land cover and emission sources on atmospheric NH_3 dynamics.

1013

1014 Overall, the synthesis of data summarized in Table 4 indicates that NH_3 concentrations in China

1015 generally range from 4 to 10 ppb, with corresponding dry deposition fluxes between 0.5 and

1016 1.0 g m^{-2} yr^{-1}. The observed variability is primarily attributed to differences in observation

1017 periods, measurement methodologies, and spatial coverage. By comparison, the United States

1018 exhibits average NH_3 concentrations of approximately 2.65 ppb and dry deposition fluxes

1019 ranging from 0.07 to 0.3 g m^{-2} yr^{-1}, while Europe reports concentrations near 3.13 ppb and

1020 deposition fluxes between 0.1 and 0.3 g m^{-2} yr^{-1}. These findings highlight that both NH_3

1021 concentrations and deposition fluxes in China are substantially higher than those reported for

1022 the United States, Europe, and global averages. Notably, Europe has integrated NH_3 control

1023 into its air pollution regulatory framework, resulting in measurable emission reductions in

1024 recent years. This experience underscores the importance of implementing more stringent NH_3

1025 mitigation policies in China to effectively address the ongoing increases in atmospheric NH_3

1026 concentrations and dry deposition fluxes.

1027

1028 Previous studies have typically examined either atmospheric NH_3 concentrations or dry

1029 deposition independently, with relatively few providing a comprehensive assessment

1030 integrating both components. This study addresses this gap by combining satellite-based lower

1031 ABL NH_3 concentrations with ground-based observations and utilizing the GEOS-Chem

1032 atmospheric chemistry transport model in conjunction with a machine learning-based Random

1033 Forest algorithm to simulate deposition velocities and fluxes. This integrated approach

1034 facilitates the generation of high-resolution, multi-year estimates of NH_3 dry deposition across

1035 China. The resulting dataset provides a robust scientific basis for improving national nitrogen

1036 management policies and offers valuable insights into regional and global nitrogen cycling

1037 processes.

1038

1039 **5 Conclusions**

1040   This study presents a comprehensive analysis of the spatial distribution and temporal trends of

1041   atmospheric ammonia (NH_3) concentrations and dry deposition across China during 2013-2023.

1042   The key findings are as follows:

1043   (1) The North China Plain exhibited persistently high NH_3 concentrations (>10 ppb), with

1044   significant annual increases in central and eastern regions (>0.4 ppb yr^{-1}). The largest seasonal

1045   increases occurred in summer (0.065 ppb yr^{-1}). NH_3 concentrations in 2023 were 13.8%-30.6%

1046   higher than in 2013 across all seasons. CrIS satellite retrievals were strongly correlated with in-

1047   situ measurements (R = 0.79), but are larger than the later by a factor of about two.

1048   (2) The spatial pattern of NH_3 dry deposition revealed a pronounced east-west gradient, with

1049   the highest flux in the North China Plain and Sichuan Basin, and a significant upward trend

1050   along the eastern coast (>0.1 g m^{-2} yr^{-1}). Over the 11-year period, NH_3 concentrations,

1051   deposition flux, and total deposition increased significantly in the land cover types of urban,

1052   cropland, and forest ecosystems. Urban areas showed the highest concentration and deposition

1053   flux as well as the fastest growth rates, while grasslands exhibited the largest total deposition.

1054   (3) The national mean NH_3 concentration and dry deposition flux were estimated to be 4.98 ppb

1055   and 0.51 g m^{-2} yr^{-1}, respectively. In addition, our analysis indicated that anthropogenic

1056   emissions were the dominant driver, accounting for approximately 77.4% of the variance in

1057 NH_3 concentrations, and meteorological conditions explained the remaining 22.6%; 72.6%-

1058   81.2% of trend for NH_3 dry deposition was governed by changes in NH_3 concentrations. These

1059   findings underscore the increasing NH_3 pollution across China and provide a critical scientific

1060   basis for informed nitrogen management within one of global largest NH_3 emission hotspots

1061   regions.

1062

1063   **Data Availability:** CrIS satellite retrievals of NH_3 were obtained from Environment and

1064   Climate Change Canada (ECCC) at

1065   https://hpfx.collab.science.gc.ca/~mas001/satellite_ext/cris/ (Shephard et al., 2015; 2020).

1066   Ground-based NH_3 measurements were sourced from Xu et al. (2019b), available at

1067   https://www.nature.com/articles/s41597-019-0061-2. NH_3 emission inventories were obtained

1068   from the Multi-resolution Emission Inventory for China (MEIC;

http://meicmodel.org.cn/?page_id=560), the Emissions Database for Global Atmospheric Research (EDGAR v8.1; https://edgar.jrc.ec.europa.eu/dataset_ap81#p3), and the Dynamic Projection model for Emissions in China (DPEC; http://meicmodel.org.cn/?page_id=1917). Emission data for SO_2 and NOx were derived from the Inversed Emission Inventory for Chinese Air Quality (CAQIEI; https://www.scidb.cn/en/detail?dataSetId=81cc0de9c68b4a4981e2f295ac612fbf), the Air Benefit and Cost and Attainment Assessment System (ABaCAS; https://abacas-dss.com/abacasChinese/Default.aspx), and the Community Emissions Data System (CEDS; https://github.com/JGCRI/CEDS/). The MEIC and EDGAR inventories were used for both NH_3 and SO_2/NOx emissions. Meteorological data were obtained from the ERA5 reanalysis dataset provided by the European Centre for Medium-Range Weather Forecasts (ECMWF) at https://cds.climate.copernicus.eu/datasets/reanalysis-era5-single-levels. The data of agricultural fertilizer application and livestock population are derived from the National Bureau of Statistics of China (https://www.stats.gov.cn/sj/ndsj/2024/indexch.htm). Agricultural zoning data were obtained from the Resource and Environmental Science Data Center (https://www.resdc.cn/Default.aspx), and land cover data were retrieved from the National Cryosphere Desert Data Center (https://www.ncdc.ac.cn/portal/metadata/9de270f3-b5ad-4e19-afc0-2531f3977f2f).

Supplement. The supplement related to this article is available online

Declaration of Competing Interest

The authors declare that they have no known competing financial interests or personal relationships that could have appeared to influence the work reported in this paper.

Author contributions: FS and CH conducted the data analysis and wrote the draft under supervision of CH, CH designed the study and revised this paper, JS and XL conducted GEOS-Chem modeling, all other co-authors collected supporting data, read and approved the final manuscript.

Acknowledgments

References:

Ai X, Hu C, Yang Y, et al. Quantification of Central and Eastern China's atmospheric CH_4 enhancement changes and its contributions based on machine learning approach. Journal of Environmental Sciences, 2024, 138: 236-248.

Asadi M, McPhedran K N. Greenhouse gas emission estimation from municipal wastewater using a hybrid approach of generative adversarial network and data-driven modelling. Science of The Total Environment, 2021, 800: 149508.

Beer R, Shephard M W, Kulawik S S, et al. First satellite observations of lower tropospheric ammonia and methanol[J]. Geophysical Research Letters, 2008, 35(9).

Behera S N, Sharma M, Aneja V P, et al. Ammonia in the atmosphere: a review on emission sources, atmospheric chemistry and deposition on terrestrial bodies. Environmental Science and Pollution Research, 2013, 20: 8092-8131.

Beusen A H W, Bouwman A F, Heuberger P S C, et al. Bottom-up uncertainty estimates of global ammonia emissions from global agricultural production systems. Atmospheric environment, 2008, 42(24): 6067-6077.

Cao C, Lee X, Liu S D, Schultz N, Xiao W, Zhang M, Zhao L. Urban heat islands in china enhanced by haze pollution. Nature Communications, 2016, 7(1): 12509. DOI:10.1038/ncomms12509

Chang, Y., Gao, Y., Lu, Y., Qiao, L., Kuang, Y., Cheng, K., Wu, Y., Lou, S., Jing, S., Wang, H., and Huang, C.: Discovery of a Potent Source of Gaseous Amines in Urban China, Environmental Science & Technology Letters, 10.1021/acs.estlett.1c00229, 2021.

Chen J, Cheng M, Krol M, et al. Trends in anthropogenic ammonia emissions in China since 1980: A review of approaches and estimations. Frontiers in Environmental Science, 2023, 11: 1133753.

1127 Chen P L, Xiao X X, Wang Q G. High-resolution characteristics of NH$_3$ emission from 2010 to 2020 in China
1128   based on satellite observation. Environmental Science, 2023, 43(6): 2673-2682.

1129 Chen Y, Shen H, Kaiser J, et al. High-resolution hybrid inversion of IASI ammonia columns to constrain US
1130   ammonia emissions using the CMAQ adjoint model. Atmospheric chemistry and physics, 2021, 21(3):
1131   2067-2082.

1132 Clarisse L, Clerbaux C, Dentener F, et al. Global ammonia distribution derived from infrared satellite
1133   observations[J]. Nature Geoscience, 2009, 2(7): 479-483.

1134 Crippa M, Guizzardi D, Pagani F, et al. Insights into the spatial distribution of global, national, and
1135   subnational greenhouse gas emissions in the Emissions Database for Global Atmospheric Research
1136   (EDGAR v8.0). Earth System Science Data, 2024, 16(6): 2811-2830.

1137 Crippa, M., Janssens-Maenhout, G., Guizzardi, D., Van Dingenen, R., and Dentener, F.: Contribution and
1138   uncertainty of sectorial and regional emissions to regional and global PM2.5 health impacts, Atmos.
1139   Chem. Phys., 19, 5165–5186, https://doi.org/10.5194/acp-19-5165-2019, 2019.

1140 Deng Z. Satellite ammonia (NH$_3$) remote sensing retrieval technology and its application in China[D], 2022.

1141 Dong J, Li B, Li Y, et al. Atmospheric ammonia in China: Long-term spatiotemporal variation, urban-rural
1142   gradient, and influencing factors. Science of The Total Environment, 2023, 883: 163733.

1143 Eastham S D, Weisenstein D K, Barrett S R H. Development and evaluation of the unified tropospheric-
1144   stratospheric chemistry extension (UCX) for the global chemistry-transport model GEOS-Chem.
1145   Atmospheric Environment, 2014, 89: 52-63.

1146 Erisman J W, Sutton M A, Galloway J, et al. How a century of ammonia synthesis changed the world. Nature
1147   geoscience, 2008, 1(10): 636-639.

1148 Evangeliou N, Balkanski Y, Eckhardt S, et al. 10-year satellite-constrained fluxes of ammonia improve
1149   performance of chemistry transport models[J]. Atmospheric Chemistry and Physics, 2021, 21(6): 4431-
1150   4451.

1151 Flechard C R, Nemitz E, Smith R I, et al. Dry deposition of reactive nitrogen to European ecosystems: a
1152   comparison of inferential models across the NitroEurope network. Atmospheric Chemistry and Physics,
1153   2011, 11(6): 2703-2728.

1154 Fu X, Wang S, Xing J, et al. Increasing ammonia concentrations reduce the effectiveness of particle pollution
1155   control achieved via SO$_2$ and NO$_x$ emissions reduction in east China. Environmental Science &
1156   Technology Letters, 2017, 4(6): 221-227.

1157   Goldberg D L, Anenberg S C, Lu Z, et al. Urban NO_x emissions around the world declined faster than

1158   anticipated between 2005 and 2019. Environmental Research Letters, 2021, 16(11): 115004.

1159   Griffis T J, Hu C, Baker J M, et al. Tall tower ammonia observations and emission estimates in the US

1160   Midwest. Journal of Geophysical Research: Biogeosciences, 2019, 124(11): 3432-3447.

1161   Hauglustaine D A, Balkanski Y, Schulz M. A global model simulation of present and future nitrate aerosols

1162   and their direct radiative forcing of climate. Atmospheric Chemistry and Physics, 2014, 14(20): 11031-

1163   11063.

1164   He K, Yang F, Ma Y, et al. The characteristics of PM2. 5 in Beijing, China. Atmospheric Environment, 2001,

1165   35(29): 4959-4970.

1166   Hernández D L, Vallano D M, Zavaleta E S, et al. Nitrogen pollution is linked to US listed species declines.

1167   BioScience, 2016, 66(3): 213-222.

1168   Hu, C, Wang Y, Wang W, et al. Trends in evaporation of a large subtropical lake. Theoretical and Applied

1169   Climatology, 2017, 129, 159–170, https://doi.org/10.1007/s00704-016-1768-z.

1170   Hu C, Griffis T J, Baker J M, et al. Modeling the sources and transport processes during extreme ammonia

1171   episodes in the US Corn Belt. Journal of Geophysical Research: Atmospheres, 2020, 125(2):

1172   e2019JD031207.

1173   Hu C, Griffis T J, Frie A, et al. A multiyear constraint on ammonia emissions and deposition within the US

1174   corn belt. Geophysical Research Letters, 2021, 48(6): e2020GL090865.

1175   Jia Y, Yu G, Gao Y, et al. Global inorganic nitrogen dry deposition inferred from ground-and space-based

1176   measurements. Scientific reports, 2016, 6(1): 19810.

1177   Kang Y, Liu M, Song Y, et al. High-resolution ammonia emissions inventories in China from 1980 to 2012.

1178   Atmospheric Chemistry and Physics, 2016, 16(4): 2043-2058.

1179   Kharol S K, Shephard M W, McLinden C A, et al. Dry deposition of reactive nitrogen from satellite

1180   observations of ammonia and nitrogen dioxide over North America. Geophysical Research Letters, 2018,

1181   45(2): 1157-1166.

1182   Lei M, Cheng T, Li X, et al. Atmospheric ammonia point source detection technique at regional scale using

1183   high resolution satellite imagery and deep learning. Atmospheric Research, 2021, 257: 105587.

1184   Liao W, Liu M, Huang X, et al. Estimation for ammonia emissions at county level in China from 2013 to

1185   2018[J]. Science China Earth Sciences, 2022, 65(6): 1116-1127.

Liu C, Huang J, Hu C. et al. Sensitivity of surface downward longwave radiation to aerosol optical depth over the Lake Taihu region, China, Atmospheric Research, 305 (2024) 107444

Liu L, Wen Z, Liu S, et al. Decline in atmospheric nitrogen deposition in China between 2010 and 2020. Nature Geoscience, 2024, 17(8): 733-736.

Liu L, Zhang X, Wong A Y H, et al. Estimating global surface ammonia concentrations inferred from satellite retrievals. Atmospheric Chemistry and Physics, 2019, 19(18): 12051-12066.

Liu L, Zhang X, Xu W, et al. Global estimates of dry ammonia deposition inferred from space-measurements. Science of the Total Environment, 2020a, 730: 139189.

Liu L, Zhang X, Xu W, et al. Ground ammonia concentrations over China derived from satellite and atmospheric transport modeling. Remote Sensing, 2017a, 9(5): 467.

Liu L, Zhang X, Xu W, et al. Reviewing global estimates of surface reactive nitrogen concentration and deposition using satellite retrievals. Atmospheric Chemistry and Physics, 2020b, 20(14): 8641-8658.

Liu L, Zhang X, Xu W, et al. Temporal characteristics of atmospheric ammonia and nitrogen dioxide over China based on emission data, satellite observations and atmospheric transport modeling since 1980. Atmospheric Chemistry and Physics, 2017b, 17(15): 9365-9378.

Liu M, Huang X, Song Y, et al. Ammonia emission control in China would mitigate haze pollution and nitrogen deposition, but worsen acid rain. Proceedings of the National Academy of Sciences, 2019, 116(16): 7760-7765.

Liu M, Huang X, Song Y, et al. Rapid SO_2 emission reductions significantly increase tropospheric ammonia concentrations over the North China Plain. Atmospheric Chemistry and Physics, 2018, 18(24): 17933-17943.

Liu S, Xu H, Wang J, et al. Evidence for global increases in urban ammonia pollution and their drivers. Science of the Total Environment, 2024, 955: 176846.

Liu, H., Hu, C., Xiao, Q., Zhang, J., Sun, F., Shi, X., Chen, X., Yang, Y., and Xiao, W.: Analysis of anthropogenic CO2 emission uncertainty and influencing factors at city scale in Yangtze River Delta region: One of the world's largest emission hotspots, Atmospheric Pollution Research, 15, 102281, https://doi.org/10.1016/j.apr.2024.102281, 2024

Lu X, Liu Y, Su J, et al. Tropospheric ozone trends and attributions over East and Southeast Asia in 1995-2019: An integrated assessment using statistical methods, machine learning models, and multiple

chemical transport models. EGUsphere, 2024, 2024: 1-65.

Lu X, Zhang L, Wu T, et al. Development of the global atmospheric chemistry general circulation model BCC-GEOS-Chem v1. 0: model description and evaluation[J]. Geoscientific model development, 2020, 13(9): 3817-3838.

Luo Z, Zhang Y, Chen W, et al. Estimating global ammonia (NH_3) emissions based on IASI observations from 2008 to 2018[J]. Atmospheric Chemistry and Physics Discussions, 2022, 2022: 1-22.

Luo, Y., Ye, X., Chuai, X. et al. Spatiotemporal patterns and carbon balance of non-grain cultivation across China: coupling coordination analysis and multi-objective optimization. Environ Dev Sustain (2025). https://doi.org/10.1007/s10668-025-06776-2

Lutsch E, Strong K, Jones D B A, et al. Unprecedented atmospheric ammonia concentrations detected in the high Arctic from the 2017 Canadian wildfires[J]. Journal of Geophysical Research: Atmospheres, 2019, 124(14): 8178-8202.

Ma S. High-resolution assessment of ammonia emissions in China: Inventories, driving forces and mitigation. Atmospheric Environment, 2020, 229: 117458.

Manisha K, Singh I, Chettry V. Investigating and analyzing the causality amid tourism, environment, economy, energy consumption, and carbon emissions using Toda–Yamamoto approach for Himachal Pradesh, India[J]. Environment, Development and Sustainability, 2025, 27(4): 8731-8766.

Na K, Song C, Switzer C, et al. Effect of ammonia on secondary organic aerosol formation from α-pinene ozonolysis in dry and humid conditions. Environmental science & technology, 2007, 41(17): 6096-6102.

Paulot F, Jacob D J, Pinder R W, et al. Ammonia emissions in the United States, European Union, and China derived by high-resolution inversion of ammonium wet deposition data: Interpretation with a new agricultural emissions inventory (MASAGE_NH_3). Journal of Geophysical Research: Atmospheres, 2014, 119(7): 4343-4364.

Phillips S B, Aneja V P, Kang D, et al. Modelling and analysis of the atmospheric nitrogen deposition in North Carolina. International journal of global environmental issues, 2006, 6(2-3): 231-252.

Pinder R W, Adams P J, Pandis S N. Ammonia emission controls as a cost-effective strategy for reducing atmospheric particulate matter in the eastern United States. 2007.

Pinder R W, Gilliland A B, Dennis R L. Environmental impact of atmospheric NH_3 emissions under present and future conditions in the eastern United States. Geophysical Research Letters, 2008, 35(12).

Santamouris M. Heat-island effect[M]//Energy and climate in the urban built environment. Routledge, 2013: 48-68.

Shao S C, Chang Y H, Cao F, et al. High-frequency evolution of urban atmospheric ammonia and ammonium and its gas-to-particle conversion mechanism in Nanjing City. Huan Jing ke Xue= Huanjing Kexue, 2019, 40(10): 4355-4363.

Shephard M W, Cady-Pereira K E, Luo M, et al. TES ammonia retrieval strategy and global observations of the spatial and seasonal variability of ammonia[J]. Atmospheric Chemistry and Physics, 2011, 11(20): 10743-10763.

Shephard M W, Cady-Pereira K E. Cross-track Infrared Sounder (CrIS) satellite observations of tropospheric ammonia. Atmospheric Measurement Techniques, 2015, 8(3): 1323-1336.

Shephard M W, Dammers E, Cady-Pereira K E, et al. Ammonia measurements from space with the Cross-track Infrared Sounder: characteristics and applications. Atmospheric Chemistry and Physics, 2020, 20(4): 2277-2302.

Shephard, Mark W., Shailesh K. Kharol, Enrico Dammers, Christopher E. Sioris, Andrew Bell, Rik Jansen, Jérôme Caron, Ralph Snel, Emanuela Palombo, Karen E. Cady-Pereira, Chris A. McLinden, Erik Lutsch, and Robert Knuteson, Infrared Satellite Detection Limits for Monitoring Atmospheric Ammonia, IEEE J. of Selected Topics in Applied Earth Observations and Remote Sensing (JSTAR), DOI: 10.1109/JSTARS.2025.3557240: 2025, 18, 10272-10291.

Someya Y, Imasu R, Shiomi K, et al. Atmospheric ammonia retrieval from the TANSO-FTS/GOSAT thermal infrared sounder. Atmospheric Measurement Techniques, 2020, 13(1): 309-321.

Song X. Study on the present situation and countermeasures of agricultural sustainable development in Huang-Huai-Hai Plain. Agricultural Science, 2024, 7(5): 74-76.

Van Damme M, Clarisse L, Franco B, et al. Global, regional and national trends of atmospheric ammonia derived from a decadal (2008-2018) satellite record. Environmental Research Letters, 2021, 16(5): 055017.

Van Damme M, Clarisse L, Whitburn S, et al. Industrial and agricultural ammonia point sources exposed. Nature, 2018, 564(7734): 99-103.

Van Der Graaf S, Dammers E, Schaap M, et al. How are NH_3 dry deposition estimates affected by combining the LOTOS-EUROS model with IASI-NH_3 satellite observations?. Atmospheric Chemistry and Physics,

1273   2018, 18(17): 13173-13196.

1274   Van Der Graaf S, Dammers E, Segers A, et al. Data assimilation of CrIS NH$_3$ satellite observations for

1275   improving spatiotemporal NH$_3$ distributions in LOTOS-EUROS. Atmospheric Chemistry and Physics,

1276   2022, 22(2): 951-972.

1277   Wang R, Pan D, Guo X, et al. Bridging the spatial gaps of the Ammonia Monitoring Network using satellite

1278   ammonia measurements. Atmospheric Chemistry and Physics, 2023, 23(20): 13217-13234.

1279   Warner J X, Dickerson R R, Wei Z, et al. Increased atmospheric ammonia over the world's major agricultural

1280   areas detected from space. Geophysical Research Letters, 2017, 44(6): 2875-2884.

1281   White E, Shephard M W, Cady-Pereira K E, et al. Accounting for non-detects: Application to satellite

1282   ammonia observations. Remote sensing, 2023, 15(10): 2610.

1283   Wu Y, Gu B, Erisman J W, et al. PM2. 5 pollution is substantially affected by ammonia emissions in China.

1284   Environmental pollution, 2016, 218: 86-94.

1285   Xi Y, Zhu J, Zhang Q, et al. Hysteresis response of wet nitrate deposition to emission reduction in Chinese

1286   terrestrial ecosystems. Atmospheric Environment, 2021, 260: 118555.

1287   Xu W, Liu X, Liu L, et al. Impact of emission controls on air quality in Beijing during APEC 2014:

1288   Implications from water-soluble ions and carbonaceous aerosol in PM$_{2.5}$ and their precursors.

1289   Atmospheric Environment, 2019a, 210: 241-252.

1290   Xu W, Luo X S, Pan Y P, et al. Quantifying atmospheric nitrogen deposition through a nationwide monitoring

1291   network across China. Atmospheric Chemistry and Physics, 2015, 15(21): 12345-12360.

1292   Xu W, Zhang L, Liu X. A database of atmospheric nitrogen concentration and deposition from the nationwide

1293   monitoring network in China. Scientific data, 2019b, 6(1): 51.

1294   Yang J, Huang X. The 30m annual land cover dataset and its dynamics in China from 1990 to 2019. Earth

1295   System Science Data, 2021, 13, (8): 3907-3925.

1296   Zavyalov V, Esplin M, Scott D, et al. Noise performance of the CrIS instrument. Journal of Geophysical

1297   Research: Atmospheres, 2013, 118(23): 13,108-13,120.

1298   Zeng Z C, Lee L, Qi C. Optimal estimation retrieval of tropospheric ammonia from the Geostationary

1299   Interferometric Infrared Sounder onboard FengYun-4B, Atmospheric Measurement Techniques

1300   Discussions, 2023, 2023: 1-24.

1301   Zhan X, Adalibieke W, Cui X, et al. Improved estimates of ammonia emissions from global croplands.

1302   Environmental Science & Technology, 2020, 55(2): 1329-1338.

1303   Zhang J, Ji D, Hu C, et al. Multiple-model based simulation of urban atmospheric methane concentration and

1304   the attributions to its seasonal variations: A case study in Hangzhou megacity, China. Environmental

1305   Pollution, 2024, 361: 124781.

1306   Zhang L, Jacob D J, Knipping E M, et al. Nitrogen deposition to the United States: distribution, sources, and

1307   processes. Atmospheric Chemistry and Physics, 2012, 12(10): 4539-4554.

1308   Zhang X, Gu B, van Grinsven H, et al. Societal benefits of halving agricultural ammonia emissions in China

1309   far exceed the abatement costs. Nature communications, 2020, 11(1): 4357.

1310   Zhang X, Wu Y, Liu X, et al. Ammonia emissions may be substantially underestimated in China[J].

1311   Environmental Science & Technology, 2017, 51(21): 12089-12096.

1312   Zheng B, Tong D, Li M, et al. Trends in China's anthropogenic emissions since 2010 as the consequence of

1313   clean air actions[J]. Atmospheric Chemistry and Physics, 2018, 18(19): 14095-14111.

1314   Zhu L, Henze D K, Bash J O, et al. Sources and impacts of atmospheric NH_3: current understanding and

1315   frontiers for modeling, measurements, and remote sensing in North America. Current Pollution Reports,

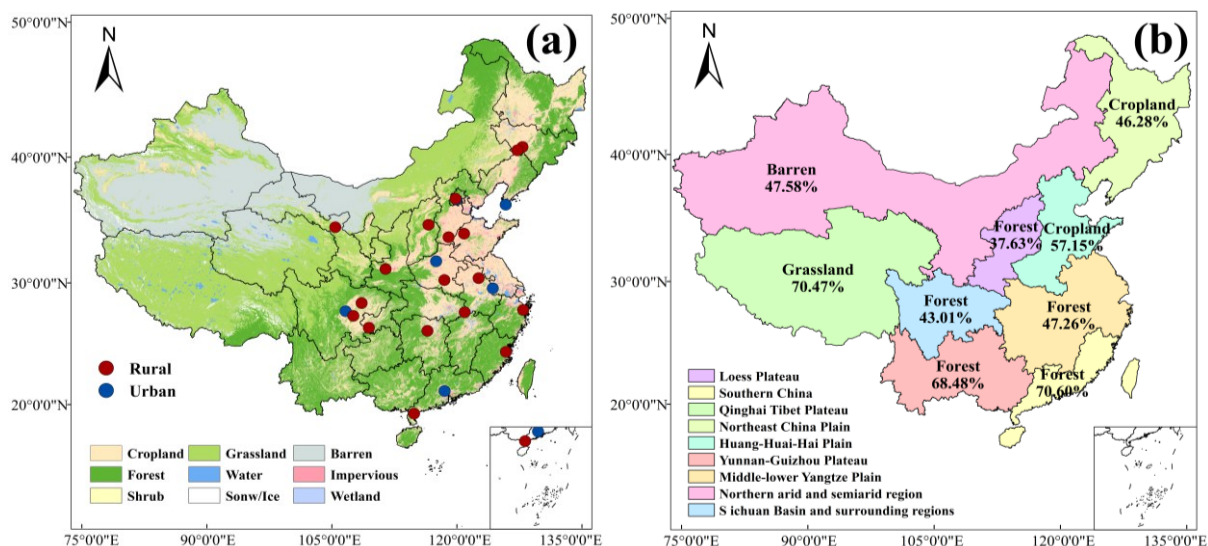1316   2015, 1: 95-116.

1317

1318

Figure 1. (a) Spatial distribution of land cover types and NH$_3$ monitoring sites in China in 2022, (b) classification of China into nine major agroecological zones based on agricultural practices and climatic conditions, note the percentage values represent area proportion of main land cover type (as list above) to total area in corresponding region.
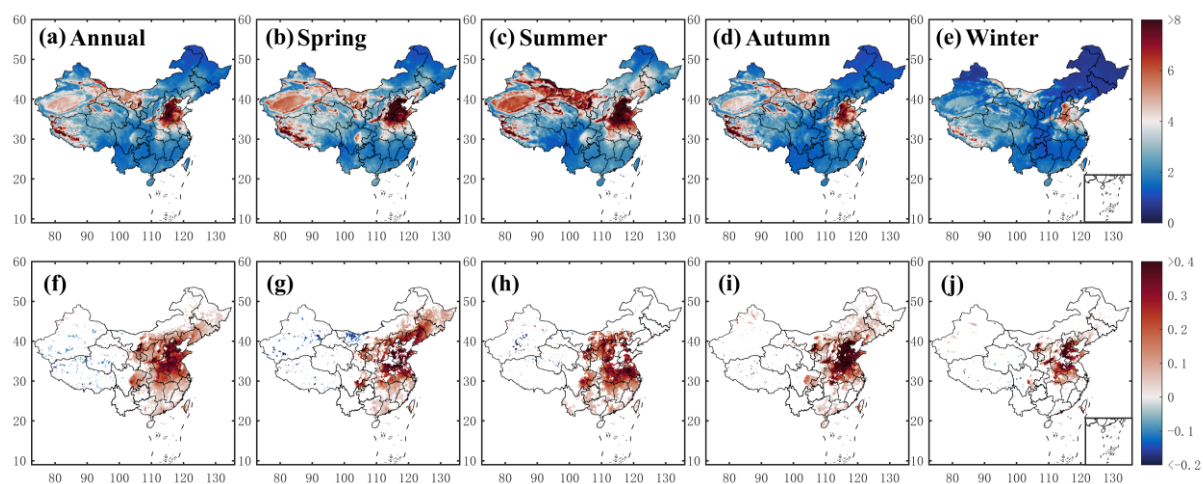
Figure 2. Spatial distribution of annual and seasonal averages of column-averaged NH_3 concentration from 2013 to 2023, (a) annual averages, (b) average in spring, (c) average in summer, (d) average in autumn, (e) average in winter; and trend of corresponding column-averaged NH_3 concentration from 2013 to 2023 for (f) annual averages, (g) average in spring, (h) average in summer, (i) average in autumn, (j) average in winter (Units: ppb for concentration; ppb yr^{-1} for trend), note the white areas in the figure indicate trends that were not statistically significant at the 0.05 level.
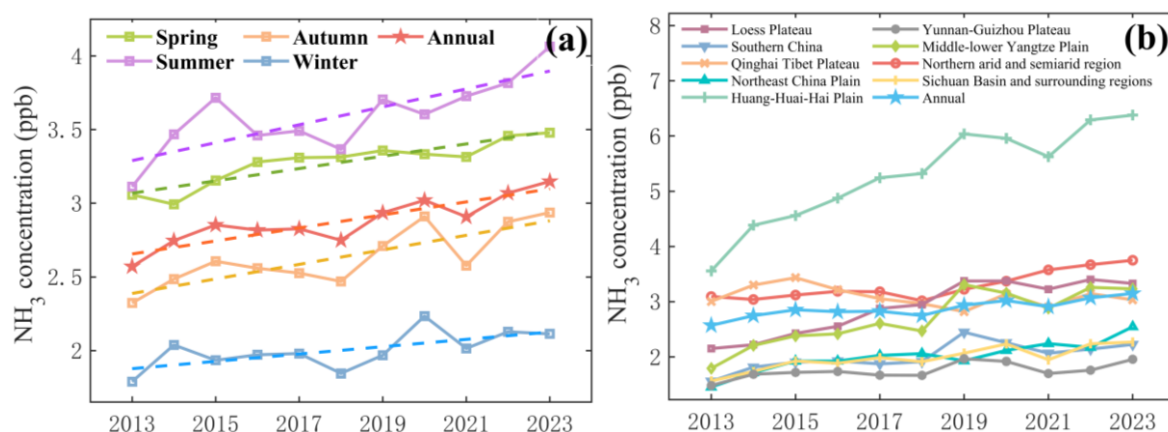
Figure 3. (a) Seasonal and (b) regional variations in CrIS satellite-based column-averaged (from ground to 1 km) NH$_3$ concentrations across China from 2013 to 2023 (Unit: ppb).
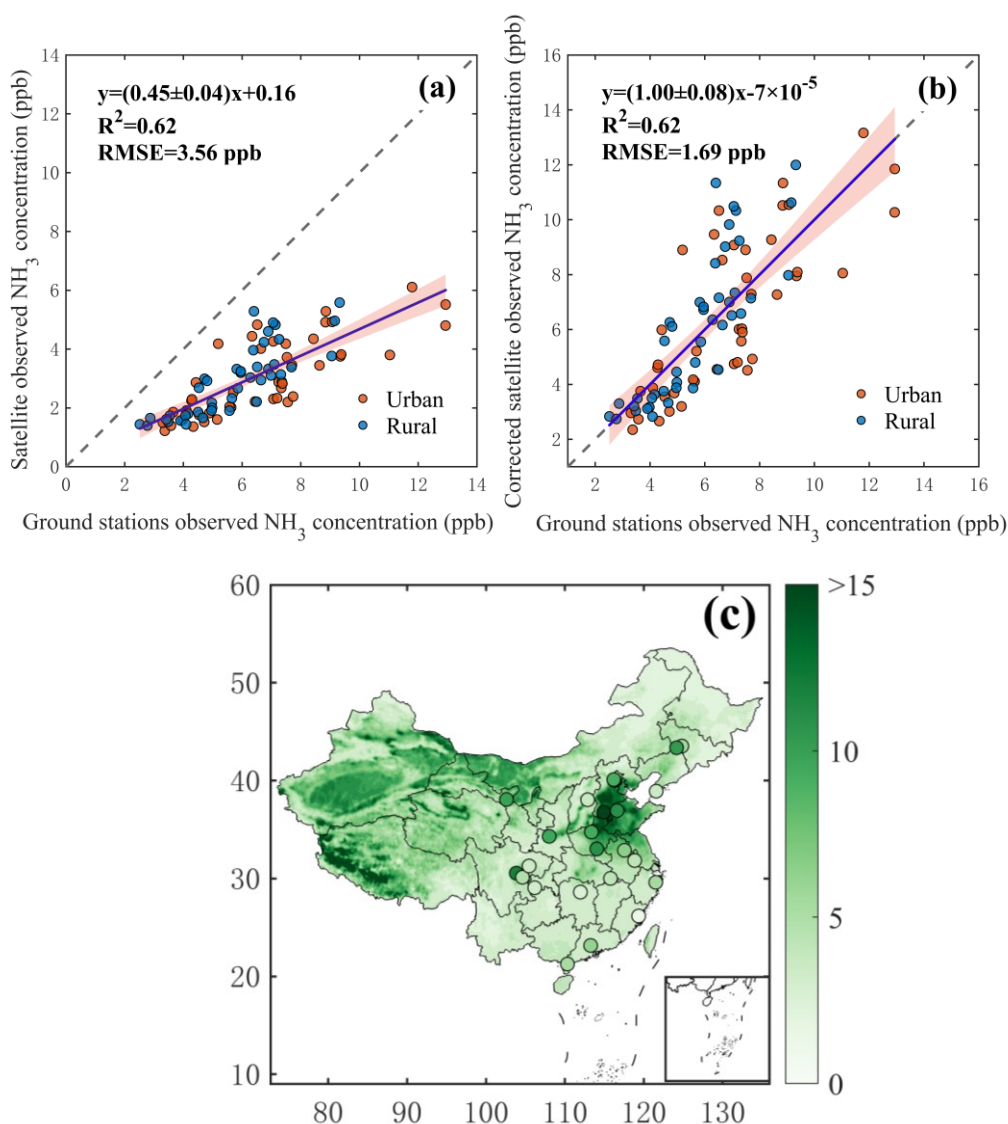
Figure 4. (a) Comparison between CrIS satellite-based column average (from ground to ~1 km) NH$_3$ concentration and ground site based (~1.5 m) NH$_3$ observations before adjustment; (b) comparison between CrIS satellite-based column average NH$_3$ concentration and ground site based NH$_3$ observations after adjustment to ground-level; (c) Spatial distribution of adjusted satellite-based NH$_3$ concentration and comparisons with ground site based NH$_3$ concentrations in 2015 (Unit: ppb), note the adjustment from CrIS satellite-based column average (ground to ~1 km) to ground-level (~1.5 m) is conducted by using the linear regression equation derived from panel a, each scatter plot represents monthly averages of all available observations for either urban or rural site.
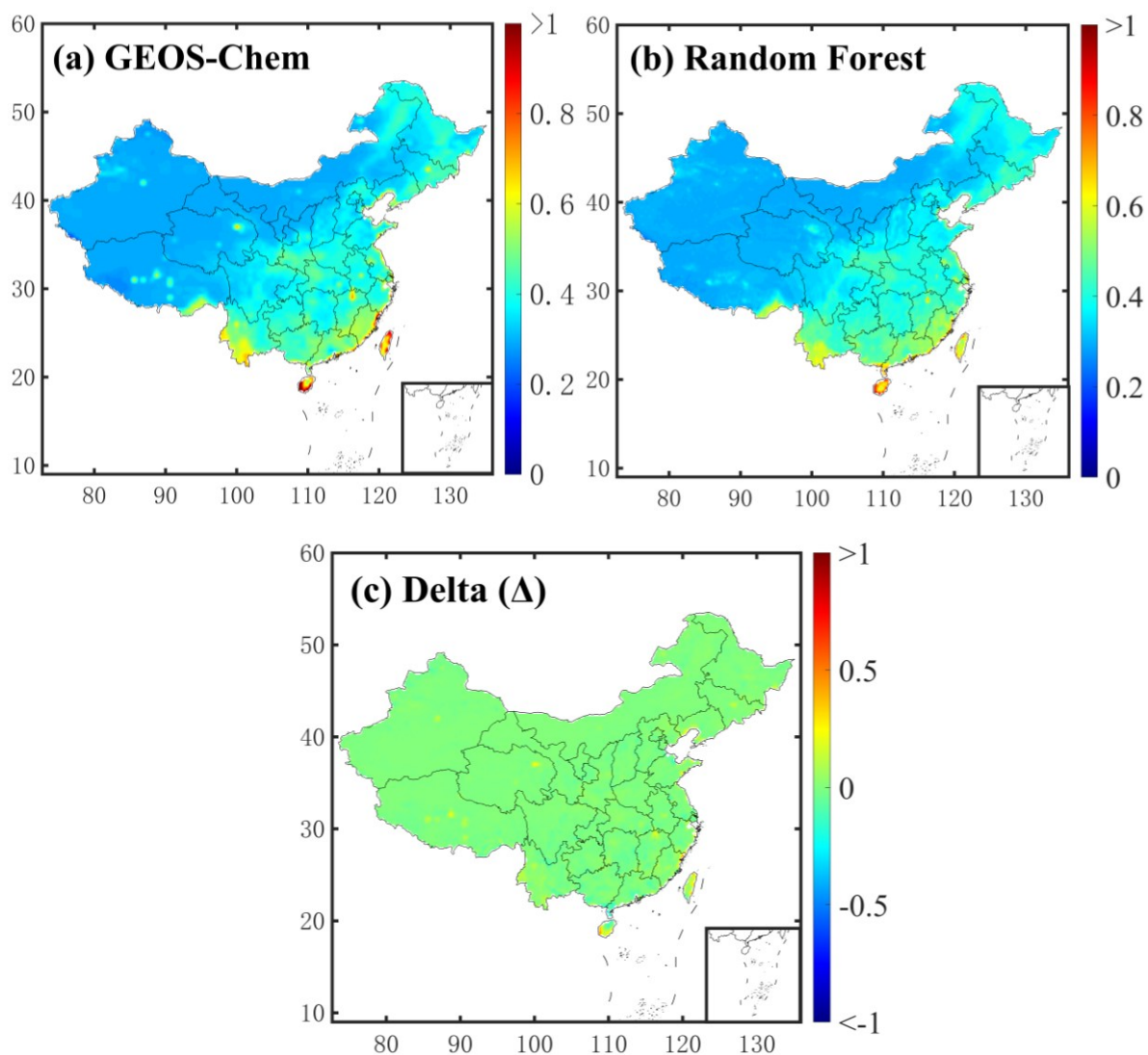
Figure 5. NH$_3$ dry deposition velocity in China in 2015: (a) GEOS-Chem simulation; (b) Random forest simulation (includes both validation set and training set); (c) Model difference (Unit: cm·s^{-1})
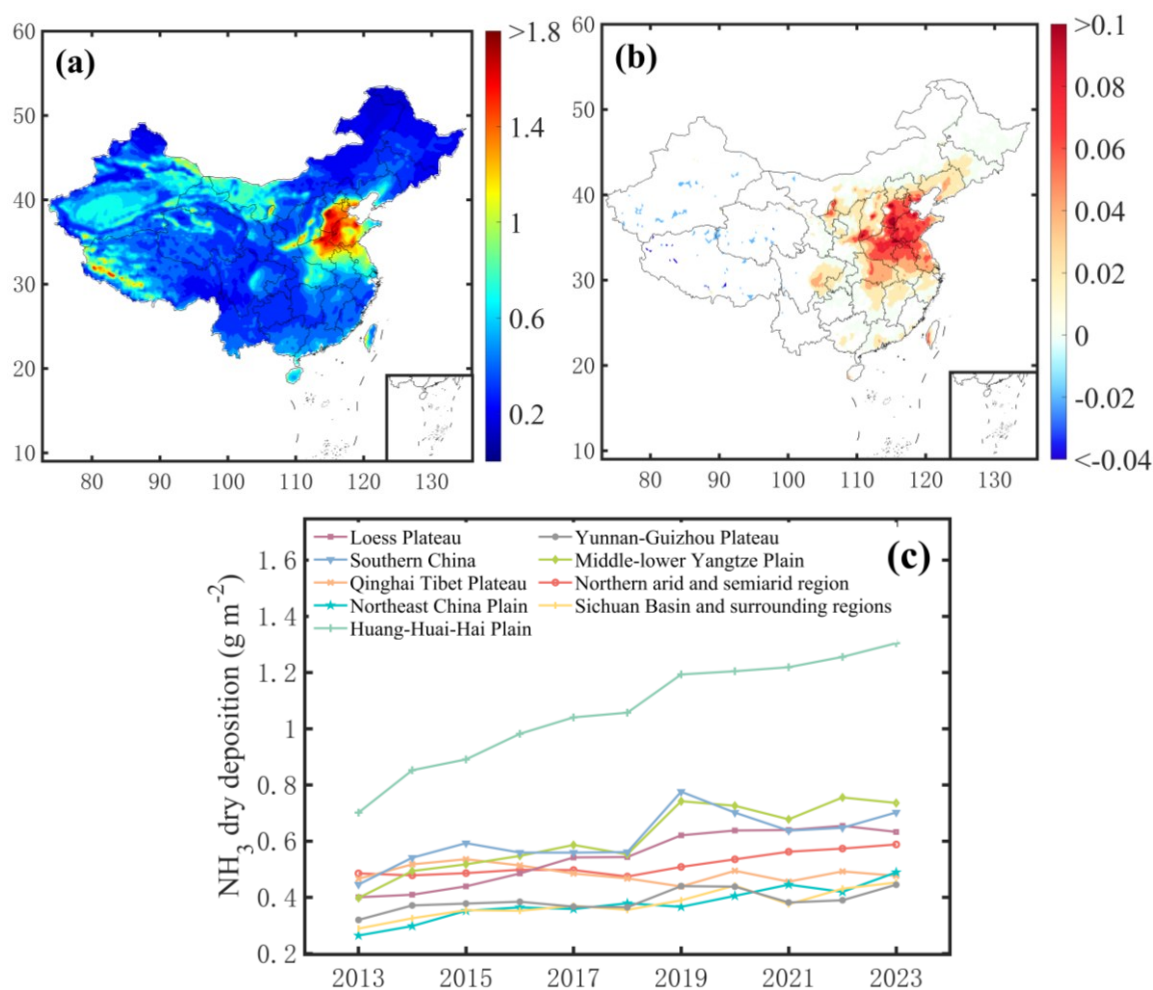
Figure 6. Spatial and regional trends in annual mean NH₃ dry deposition in China from 2013 to 2023: (a) spatial distribution of annual mean NH₃ dry deposition (Unit: $g \cdot m^{-2}$); (b) temporal trend of NH₃ dry deposition (Unit: $g \cdot m^{-2} \cdot yr^{-1}$); (c) interannual variation of NH₃ dry deposition across different regions (Unit: $g \cdot m^{-2}$).
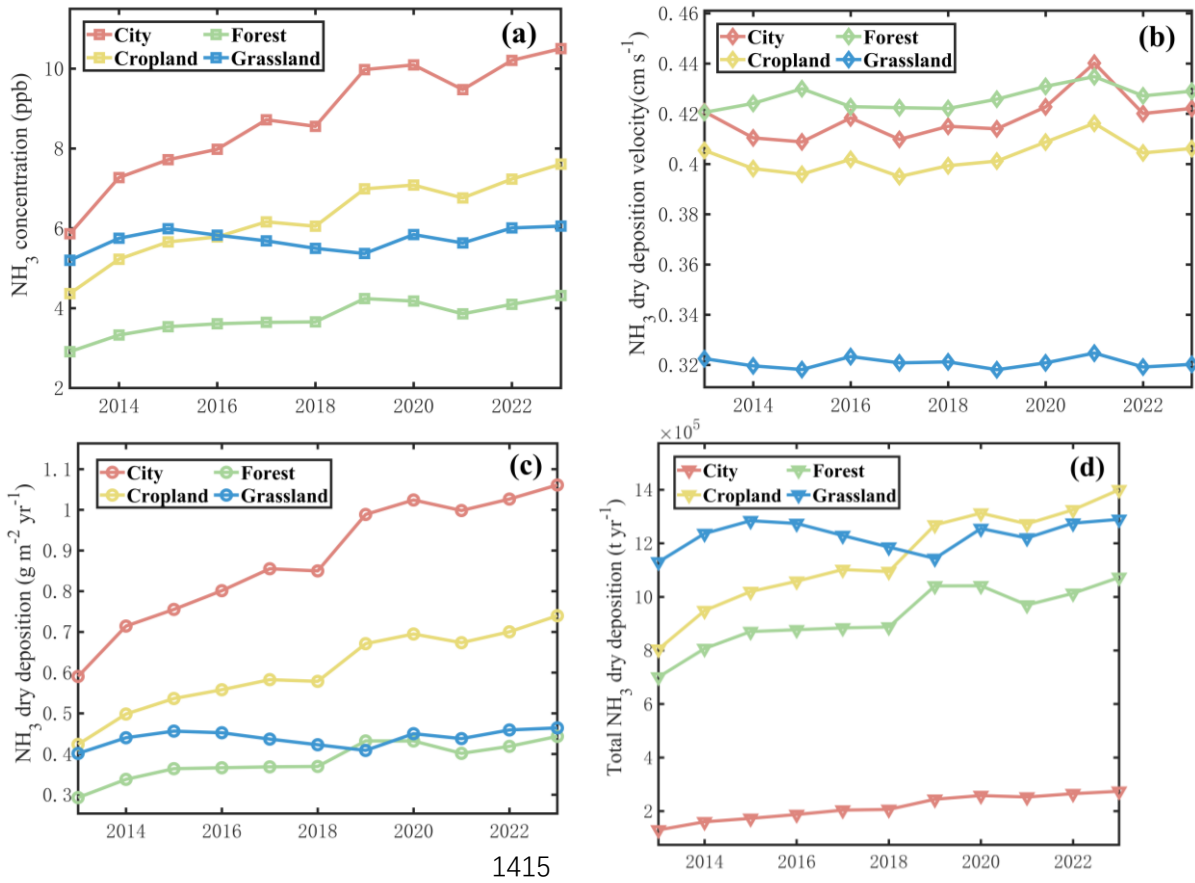
1415

Figure 7. Trends in NH₃ concentration, dry deposition velocity, and dry deposition amount in China from 2013 to 2023: (a) trends in corrected NH₃ concentrations across different land surface types (Unit: ppb); (b) NH₃ dry deposition velocities over different land surface types (Unit: cm·s⁻¹); (c) trends in NH₃ dry deposition flux per unit area over different land surface types (Unit: g·m⁻²); (d) interannual variation in annual NH₃ dry deposition over different land cover types (Unit: t yr⁻¹).

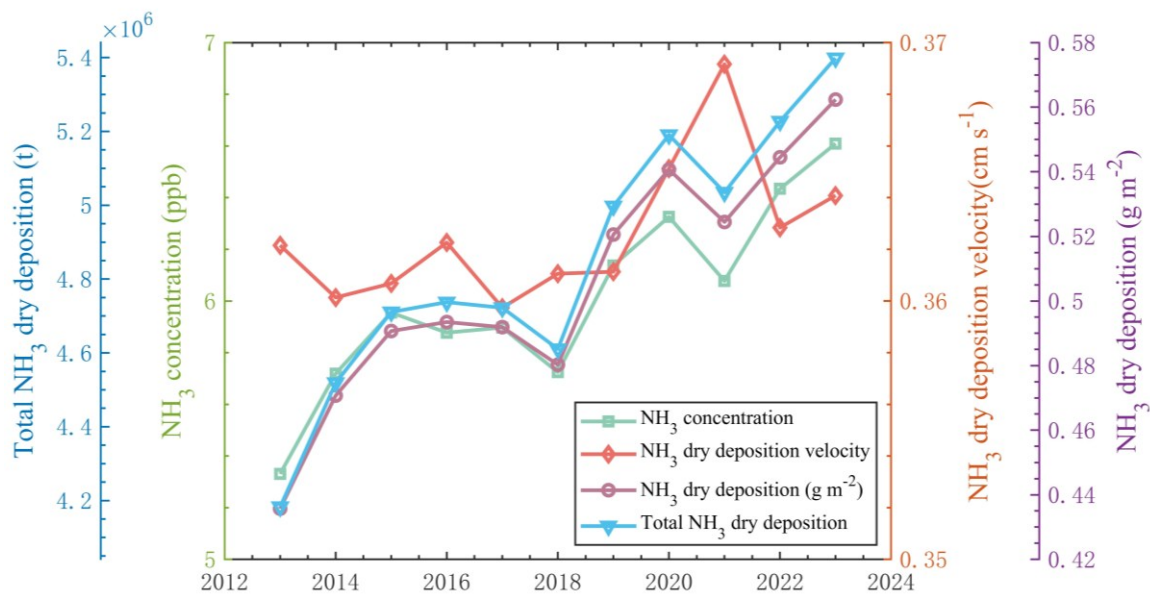**Figure 8.** Annual changes in NH₃ concentration, dry deposition velocity, dry deposition flux and total dry deposition for China from 2013 to 2023.
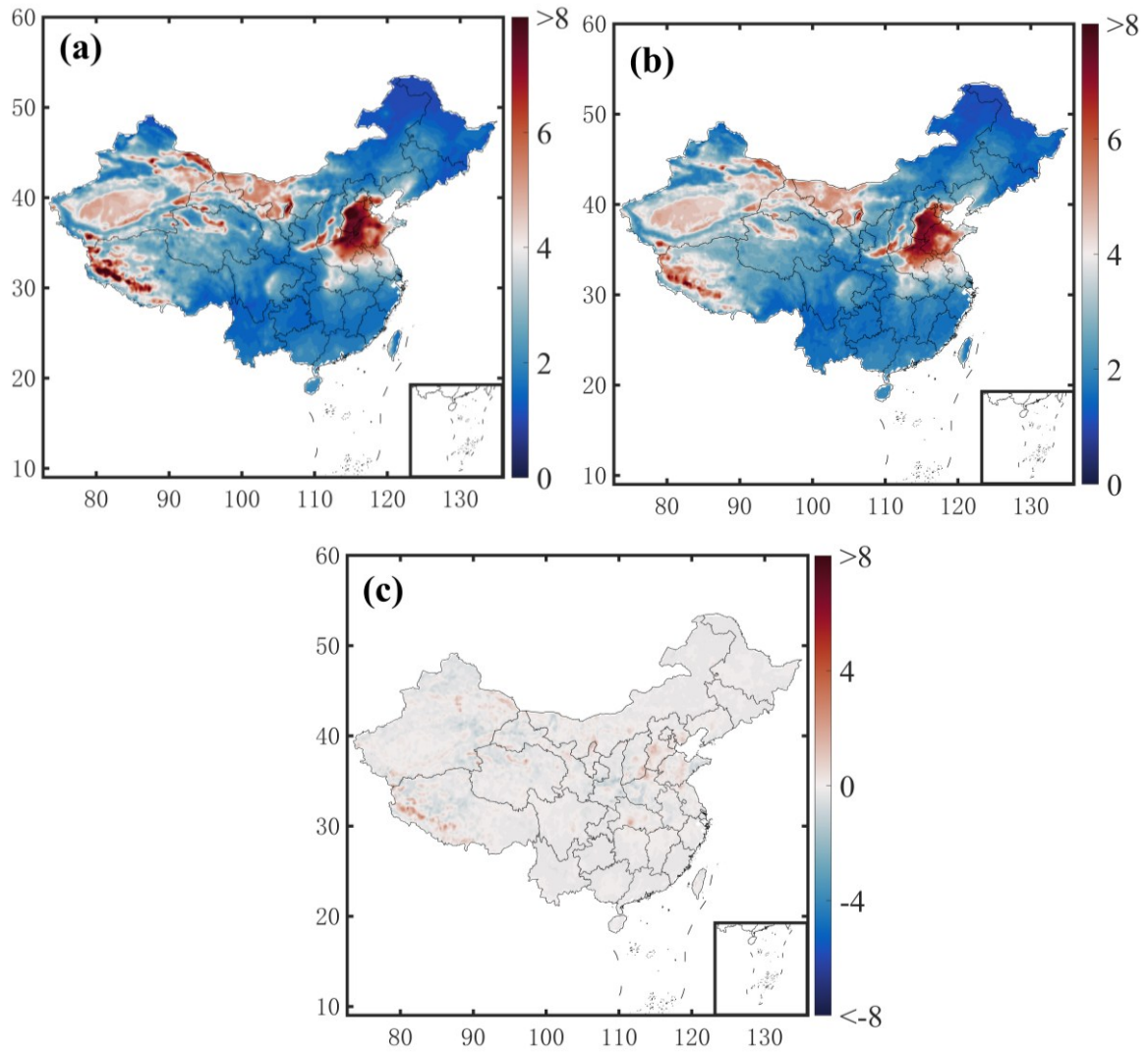
Figure 9. (a) Spatial distribution of adjusted ground-level NH_3 concentration for averages between 2013 and 2023, (b) simulation of adjusted ground-level NH_3 concentration by RF model for averages between 2013 and 2023, (c) difference between panel a and b, Units: ppb.
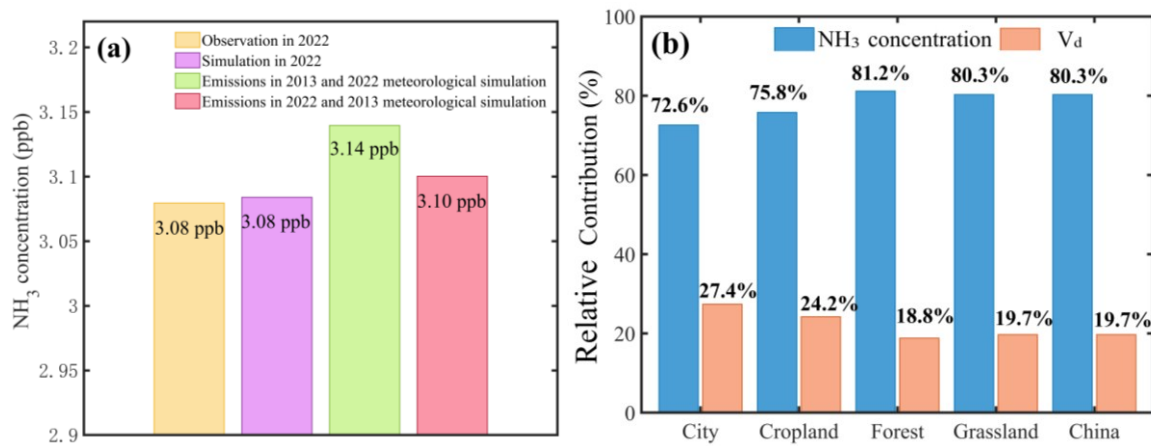
Figure 10. (a) Adjusted ground-level NH_3 concentrations and simulations by random forest models under different meteorological and emission scenarios in 2022; (b) Relative contribution of NH_3 concentration and dry deposition velocity to the dry deposition flux changes. Note: in panel a, the yellow bar represents the adjusted ground-level NH_3 concentration in 2022, the purple bar represents the random forest model simulated NH_3 concentration, the green bar represents the simulated NH_3 concentration using 2013 emissions and 2022 meteorological data, and the red bar represents the simulated NH_3 concentration using 2013 meteorological data and 2022 emissions data. And in panel b, the relative contributions of meteorological factors and emissions can be obtained by comparison with the difference in NH_3 concentration in the purple bar graph.)

1471 **Table 1.** Annual and seasonal average NH_3 concentrations and their annual mean increment and
1472 relative growth rate during entire study period.

Season	NH_3 concentration (ppb)	Annual growth in NH_3 concentration (ppb yr^{-1})	Relative annual growth rates (%)
Annual	2.88	0.045	22.5
Spring	3.28	0.039	13.8
Summer	3.59	0.065	30.6
Autumn	2.63	0.050	26.4
Winter	2.00	0.023	18.1

1473

1474

1475

1476

1477

1478

1479

1480

1481

1482

1483

1484

1485

1486

1487

1488

1489

1490

1491

1492

1493

1494

1495 **Table 2.** Average NH$_3$ concentration per unit area and annual mean increment and corrected

1496 NH$_3$ concentration in the nine major agricultural regions of China from 2013 to 2023.

Agricultural zoning	NH$_3$ concentration (ppb)	Annual growth in NH$_3$ concentration (ppb yr^{-1})	Relative annual growth rates (%)	Corrected NH$_3$ concentration (ppb)
Huang-Huai-Hai Plain	5.29	0.24	79.4	11.36
Northern arid and semiarid region	3.29	0.08	21.3	6.93
Qinghai Tibet Plateau	3.09	-0.03	0.9	6.48
Loess Plateau	2.90	0.14	54.8	6.05
Middle-lower Yangtze Plain	2.70	0.13	80.5	5.62
Southern China	2.01	0.06	42.7	4.09
Northeast China Plain	2.01	0.08	75.1	4.09
Sichuan Basin and surrounding regions	1.98	0.06	45.1	4.02
Yunnan-Guizhou Plateau	1.75	0.03	31.9	3.52

1497

1498

Table 3. Average NH$_3$ dry deposition per unit area and annual mean increment in the nine major

agricultural regions of China from 2013 to 2023.

Agricultural zoning	Dry deposition of NH$_3$ (g m^{-2})	Annual growth of NH$_3$ dry deposition (g m^{-2} yr^{-1})
Huang-Huai-Hai Plain	1.06	0.054
Northern arid and semiarid region	0.61	0.012
Qinghai Tibet Plateau	0.61	-0.004
Loess Plateau	0.55	0.030
Middle-lower Yangtze Plain	0.52	0.034
Southern China	0.49	0.020
Northeast China Plain	0.39	0.018
Sichuan Basin and surrounding regions	0.38	0.014
Yunnan-Guizhou Plateau	0.38	0.008

1501

1502

1503

1504

1505

1506

1507

1508

1509

1510

1511

1512

1513 **Table 4.** Comparison of global and regional NH$_3$ concentrations and dry deposition rates across

1514 different studies. note: All results have been standardized to uniform units.

Reference	Study period	Study region	NH$_3$ dry deposition (g m^{-2} yr^{-1})		NH$_3$ concentration (ppb)	
This study	2013-2023	China	City	0.88	City	8.76
			Forest	0.38	Forest	3.76
			Cropland	0.61	Cropland	6.27
			Grassland	0.44	Grassland	5.72
			China	0.51	China	4.98
		Global	0.17		--	
		China	0.58		Crop	8.04
					Urban	6.86
					Forest	4.66
					Grass	3.10
					Grass	3.37
					Mean	4.15
Liu et al., 2020a	2008-2016	Europe	0.36		Crop	4.00
					Urban	4.52
					Forest	3.32
					Grass	2.34
					Grass	1.87
					Mean	3.13
		US	0.26		Crop	4.38
					Urban	3.10
					Forest	2.51
					Grass	2.91
					Grass	1.87
					Mean	2.65
Jia et al., 2016	2005-2014	Asia (China)	0.29 (0.68)		--	
		North America	0.042 (0.078)		--	

Reference	Period	Region			
		(US)			
		Europe	0.11	--	
		Africa	0.32	--	
		South America	0.12	--	
		Oceania	0.037	--	
		Global land	0.18	--	
Kharol et al., 2018	2013 warm season (April-September)	North America	0.06-1.22	--	
		USA	0.27	--	
		Canada	0.18	--	
Zhang et al. 2012	2006-2008	US	0.11	--	
Liu et al., 2019	2008-2016	China	--	4.15 (0.39-22.90)	
		Europe	--	3.14 (0.07-16.58)	
		US	--	2.66 (0.24-18.52)	
Xu et al., 2015	2010-2014	China	1.00 (0.06-1.95)	10.65 (0.52-22.89)	
Phillips et al., 2006	1999 Summer	North Carolina	0.36	--	
Hu et al., 2020	November 2017	Tall-tower (100 m) observations in Minnesota — Forested lands	0.10-0.16	56 m	6.76
		Agricultural lands	0.41-0.62	100 m	6.64
Shao et al., 2019	October - November 2018	Nanjing	--	21.96±9.61	
Hu et al., 2021	2017-2019 warm season	US Corn Belt — Forested lands	0.054±0.0054, 0.059±0.011, 0.059±0.011	Forested lands 0.58±0.12, 0.71±0.14, 0.60±0.12	
		Agricultural lands	0.77±0.16, 0.76±0.16, 0.77±0.16	Agricultural lands 6.87±1.4, 6.76±1.4, 6.48±1.3	

| Van Der Graaf et al., 2018 | 2014 warm season | Europe | LOTOS-EUROS model | 0.21 | -- |
| | | | IASI | 0.27 | |

1515

1516

1517

1518

1519

1520

1521